ELSEVIER

Journal of Fluids and Structures 20 (2005) 373–402

JOURNAL OF FLUIDS AND STRUCTURES

www.elsevier.com/locate/jfs

Three-dimensional wake effects on flow-induced forces

R.M.C. So*, Y. Liu, Z.X. Cui, C.H. Zhang, X.Q. Wang

Department of Mechanical Engineering, The Hong Kong Polytechnic University, Hung Hom, Kowloon, Hong Kong

Received 17 June 2004; accepted 2 December 2004

Abstract

Numerical simulations are carried out for a long slender rigid circular cylinder in a cross-flow to examine three-dimensional (3-D) wake effects on the flow-induced forces. The aim is to assess the validity and extent of the two-dimensional (2-D) assumption for both the mean drag and the flow-induced forces. In order to simulate the practical situation correctly, wall boundary conditions are specified at both ends of the cylinder. The long slender cylinder has different aspect ratios. A finite volume method (FVM) and a lattice Boltzmann method (LBM) are used to carry out the computations, and their results are compared with each other and with available experimental and simulation data. As a first attempt to assess the 2-D assumption, a Reynolds number $\mathrm{Re} = 100$ and an aspect ratio $a = 16$ are chosen. At this Re and a, conventional experimental and numerical studies assume that the time-averaged flow is homogeneous and 2-D over a relatively large portion of the central span. However, present simulations indicate that vortex shedding from the nominally 2-D cylinder strongly depends on the span location and the flow-induced forces exhibit strong three dimensionality. The calculated mean drag and root-mean-square lift and drag vary greatly along the span. These results indicate that the 2-D assumption is not valid for the flow-induced forces, not even within a small region of the central span, for the aspect ratio examined. The validity and extent of the periodic boundary conditions assumption for a 3-D simulation of the flow and induced forces on a cylinder in a cross-flow is examined next. It is found that, within the range of a investigated, an appropriate period could not be found for the numerical simulation. The results further show that a has a significant effect on the calculated wake flow and the flow-induced forces.

Keywords: Three-dimensional vortex-induced forces, flow around 3-D cylinder, 3-D wake

1. Introduction

A three-dimensional (3-D) finite cylinder in a cross-flow is one of the most basic and revealing cases in the general subject of fluid–structure interactions. Structural vibration strongly depends on the magnitude and distribution of the unsteady flow-induced forces along the span. Numerous experimental investigations have been carried out on this problem. Important findings and understanding have been achieved on the flow-induced forces, such as their variations with Reynolds numbers and free stream turbulence (Richter and Naudascher, 1976; So and Savkar, 1981), and their dependence on the aspect ratio $a = L/D$ of the bluff body (Baban and So, 1991); and on the 3-D nature of the wake flow, such as oblique and parallel vortex shedding patterns (Williamson, 1989), cellular shedding and associated vortex

*Corresponding author. Tel.: +852 2766 7814; fax: +852 2365 4703.
E-mail address: mmmcso@polyu.edu.hk (R.M.C. So).

0889-9746/$ - see front matter © 2005 Elsevier Ltd. All rights reserved.
doi:10.1016/j.jfluidstructs.2004.12.002

dislocations (Eisenlohr and Eckelmann, 1989; Köng et al., 1990; Williamson, 1992); and different instability modes (Williamson, 1988, 1996a). Here, L is the span and D is the diameter of the cylinder. A comprehensive review of recent advances has been given by Williamson (1996b) and Zdravkovich (1997), and the more general bluff body wake has been reviewed by Roshko (1993) and Matsumoto (1999). These studies generally agree that the cylinder wake is 2-D at $\mathrm{Re} = U_\infty D/\nu = 100$ (Zhang and Dalton, 1998), where Re is the Reynolds number, U_∞ is the free-stream velocity, and ν is the fluid kinematic viscosity. Even in experimental visualization, three dimensionality cannot be identified for $\mathrm{Re} < 150$ (Hama, 1957). However, in recent studies (Szepessy and Bearman, 1992), it has been found that end conditions have a significant influence on vortex formation and their shedding from the bluff body, and on the 3-D nature of the wake flow.

Oblique shedding is one of the more important 3-D features that could influence the amplitude, frequency and phase of the flow-induced forces. The shedding pattern, either oblique or parallel, strongly depends on the boundary conditions at both ends of the span (Berger and Wille, 1972). For a circular cylinder with finite a and low Re, vortex shedding at midspan is influenced by the boundary conditions. Using a flow visualization technique, Slaouti and Gerrard (1981) examined the end effect on the wake of circular cylinders having $a = 25$–30. The cylinder was towed through a water tunnel over a range of $\mathrm{Re} = 60$–200. They reported that both free ends and end plates have severe effects on the bending of the vortex lines at the cylinder and end plate corner. When the bending of the vortex line is strong towards both ends, straight and parallel shedding is obtained in the central region. Therefore, they concluded that slantwise (oblique) shedding might not be an intrinsic feature of the wake of bluff bodies at low Re, but could be attributed to end flow conditions. Gerich and Eckelmann (1982) examined the vortex shedding frequency along a circular cylinder with free ends or end plates in a wind tunnel. They divided the cylinder span into two regions according to the extent of the influence of the end condition on the shedding frequency. In the affected region, the shedding frequency is significantly influenced by the end condition and the Strouhal number, $\mathrm{St} = \Omega_s D/U_\infty$, is about 10–15% less than that measured in the unaffected region. Here, Ω_s is the vortex shedding frequency.

Stager and Eckelmann (1991) found that the size of the affected region varies with Re, e.g., it is about $10D$ at $\mathrm{Re} = 100$ and about 5D at $\mathrm{Re} = 300$–5000. Furthermore, the size is found to decrease with increasing Re. At the boundary of the affected and unaffected regions, neighboring cells of different shedding frequencies cannot match with each other, thus, resulting in a modulation of the shedding frequency and a dislocation of the large-scale vortex in the wake flow. The effect of a on the shedding pattern and on the flow-induced forces at higher Re were carried out by West and Apelt (1982) at $\mathrm{Re} = 10^4$–10^5, by Baban and So (1991) at $\mathrm{Re} = 4.6 \times 10^4$ and by Szepessy and Bearman (1992) at $\mathrm{Re} = 8 \times 10^3$–$1.5 \times 10^5$. At lower Re, end effects are more pronounced than that at higher Re, due to the larger size of the affected region. Norberg (1994) measured the wake flow of circular cylinders with finite a at $\mathrm{Re} = 50$–4×10^4; however, he only focused on St and the suction coefficient at midspan.

Compared to experimental investigations, there were relatively few numerical studies on the 3-D nature of bluff body wakes and the flow-induced forces. On the other hand, simulations of the corresponding 2-D flow around the long slender cylinder and the associated flow-induced forces have been amply carried out (Norberg, 2003). Most of the numerical simulations rely on the continuum model described by the Navier–Stokes equations. The flow field parameters, either in the form of primitive variables, including flow velocity and pressure, or in the form of stream and vorticity functions, are solved using various discretization techniques, such as the spectral element method (Karniadakis and Triantafyllou, 1992; Thompson et al., 1994; Evangelinos and Karniadakis, 1999), the finite element method (Mittal and Balachandar, 1995), and the finite volume method (Persillon and Braza, 1998). These 2-D and 3-D simulations (Norberg, 2003) provide valuable time series for the mean and fluctuating forces and for the velocity field in the wake flow. Besides, the simulations also provide a novel way to understand the physics of wake transition. Details available from these numerical studies have contributed to a remarkable understanding of the fluid dynamics of 2-D and 3-D cylinder wakes.

Most of the 3-D numerical studies invoked periodic boundary conditions at both ends of the cylinder, thus tacitly assuming the spanwise variations to have a certain period that is specified *a priori*. These studies could provide an approximate model for the midspan wake flow, but fail to take the end effects into account. Only very few calculations have attempted to consider the effect of end flow on the 3-D wake. Schafer and Turek (1996) gave an overview of benchmark computations for 2-D and 3-D laminar flow around a cylinder with $a = 4$. Mittal (2001) used a finite element method to calculate the 3-D flow past a circular cylinder with end plates and $a = 16$. However, an assumption of a plane of symmetry at midspan was invoked. This assumption is made in spite of the large body of data showing that the wake behind the cylinder is 3-D and varies along the span. Only results at midspan were given and variation along the span was not reported. Direct numerical simulation (DNS) employing a spectral method was used to calculate the wake flow and the unsteady forces on a stationary rigid cylinder assuming periodic boundary conditions (Evangelinos and Karniadakis, 1999). Again, only results at midspan were given and no spanwise variation of the unsteady forces was reported. In all these calculations, the flow-induced forces were tacitly assumed to be stationary after the transient period has elapsed. Therefore, these data are inappropriate to use in carrying out an investigation of 3-D wake effects on the behavior of the flow-induced forces, if any.

Norberg (2003) gave a very detailed compilation of the calculated and measured fluctuating lift data for 2-D and 3-D cylinders. The collected data covered a Re range of 60–1.39×10^6 for experimental investigations and 45–4.4×10^4 for numerical simulations. Most of the 2-D simulations were carried out for $Re = 100$, while most of the 3-D calculations were performed at $Re \geqslant 1000$. Data collected include blockage, the computational domain specified for the upstream and downstream region of the cylinder, the numerical methods used to carry out the simulation, a, and C'_L, the root-mean-square of C_L. Here, C_L is defined as the unsteady lift force coefficient. The numerical methods used include finite element, finite volume, finite difference, spectral element, discrete vortex, and lattice Boltzman. These results show that, for 2-D simulations at $Re = 100$, the calculated C'_L at midspan lies in the range 0.17–0.52, with most of the values reported around 0.21–0.24. For 3-D simulations at about the same Re, the calculated C'_L at midspan varies from 0.23 to 0.27 under an assumption of periodic flow over an effective span of 2.25–11. The spanwise variation of C'_L for all these investigations was not reported. Based on these results, it appears that C'_L varies slightly between the 2-D and 3-D simulations, irrespective of the assumed effective span between the imposed periodic boundary condition, the numerical method employed, the aspect ratio of the cylinder, the computational domain specified for the upstream and downstream region, and the blockage specified. These simulation results are a lot higher than the measurements reported by Tanida et al. (1973) at $60 \leqslant Re \leqslant 110$ and by Khalak and Williamson (1996) at $Re = 200$. Therefore, the reliability of the 3-D calculations at $Re = 100$ needs further investigation.

In resolving flow-induced vibration problems, it is important to have information on the distribution of the flow-induced forces along the span of the structure. If the force does not vary along the span, a relatively simple model, such as a spring–damper–mass model could be used to analyze the structural dynamics and vibration (Zhou et al., 1999; So et al., 2001). On the other hand, if the force varies along the span, an Euler–Bernoulli or a Timoshenko beam theory with nonuniform force distribution has to be used instead, because the local fluctuating force influences the vibration mode and amplitude (Chan and Wang, 1997; Wang et al., 2001). The above review indicates that the wake is most likely 3-D above $Re = 100$. However, in most numerical treatments of flow-induced vibration problems, a full 3-D treatment of the structural dynamics using flow data derived from a full 3-D wake flow has not been reported. Even the DNS simulations (Evangelinos and Karniadakis, 1999) were carried out assuming periodic boundary conditions; hence, they did not represent a full 3-D treatment of the flow and structural dynamics simultaneously. In view of this, before attempting to calculate flow-induced vibration problems involving long slender structures, the fundamental wake flow and the distribution of the flow-induced forces along the span of a 3-D stationary rigid slender cylinder have to be resolved. The present paper attempts to answer some of these questions and provide numerical data on the spanwise variation of the flow-induced forces on the cylinder.

A common approach in past treatments of this fairly fundamental bluff body flow problem is to assume the time-averaged flow to be homogeneous along the span, at least within a finite central span region, for a long slender structure where a is relatively large. The flow across the central region is taken to be 2-D in the mean sense and is independent of the actual span of the cylinder (Norberg, 2003). In the present approach, focus is placed on the wake behind a structure having a relatively large a, and on the variation of the spanwise flow-induced forces. In order not to invoke periodic boundary conditions, a 3-D circular cylinder with end walls in a cross-flow with $a = 16$ and $Re = 100$ is numerically studied in detail. Also, calculations at the same Re but different a are carried out. At this Re and the range of a investigated, the wake flow might not be 2-D. Therefore, the first objective of the present approach is to allow the wake to evolve, be it 2-D or 3-D. It is hoped that, through this investigation, the effect of a 3-D wake on the distribution of the flow-induced forces along the cylinder span, if any, could be assessed. The second objective is to use the numerical results to attempt a resolution of the inconsistency shown in the measured and calculated data for 2-D and 3-D cylinders at $Re = 100$ (Norberg, 2003). Finally, the third objective is to assess, if possible, the validity and extent of the periodic boundary conditions assumption on a 3-D simulation of the flow and induced-forces on a cylinder in a cross-flow.

2. Numerical methods

2.1. Problem description

A schematic view of the problem is illustrated in Fig. 1(a). The rigid circular cylinder with aspect ratio a is bounded by two parallel end walls and is exposed to a cross-flow. Incompressible flow with constant fluid density ρ and constant dynamic viscosity μ is assumed. A Cartesian coordinate system (x, y, z), where the x-axis is aligned with the incoming flow direction (streamwise direction), the y-axis is perpendicular to the plane containing the streamwise and spanwise direction (z-axis), is used to describe the flow. The z-axis is chosen to coincide with the cylinder axis; hence, the origin of

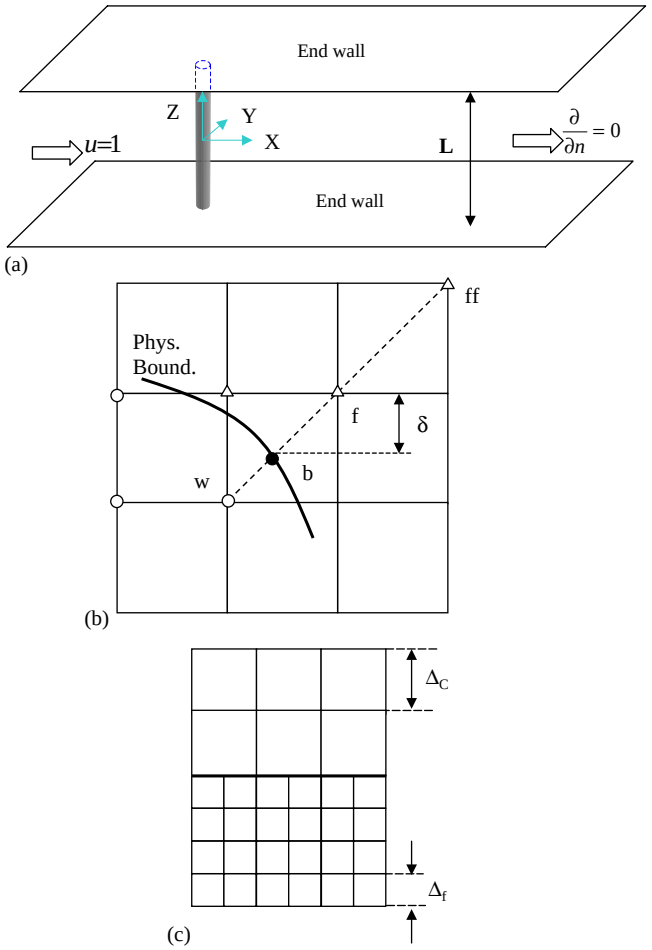

Fig. 1. (a) A schematic view of the problem; (b) uniform lattice and curved boundary; (•, boundary node; Δ fluid node; ○, solid node); (c) layout of coarse, fine lattices and their interface.

the coordinate system is located on this axis. These are dimensional physical coordinates. Two rectangular end walls are placed at the cylinder ends; therefore, the z-axis is bounded by the span of the cylinder, while the y-axis extends to infinity on both sides of the central plane. However, for computational convenience, the y extent is chosen to be at a distance where the flow is essentially parallel to the x–z plane and the velocity is the same as the incoming free-stream velocity U_∞. All physical parameters are normalized by D, ρ, μ and U_∞. The normalized flow-induced force coefficient acting on the cylinder axis is decomposed into a drag coefficient $C_D\ (0,0,Z,t)$ and a lift coefficient $C_L\ (0,0,Z,t)$, where the nondimensional time is defined as $t = \tilde{t}U_\infty/D$, and the nondimensional coordinates are denoted by $X = x/D$, $Y = y/D$ and $Z = z/D$. Here, the tilde (∼) is used to denote the dimensional counterpart of p, $\mathbf{u}$ and t. From this point on, the drag and lift coefficients, $C_D\ (Z,t)$ and $C_L\ (Z,t)$, can be written as

$$(C_D(Z,t), C_L(Z,t)) = \frac{2}{D}\oint\left(-p\mathbf{n} + \frac{1}{\mathrm{Re}}(\nabla\mathbf{u} + \nabla\mathbf{u}^{\mathrm{T}})\cdot\mathbf{n}\right)\mathrm{d}s, \tag{1}$$

where $p = \tilde{p}/\rho U_\infty^2$ and $\mathbf{u} = \tilde{\mathbf{u}}/U_\infty$ are the dimensionless static pressure and velocity vector, respectively, $\mathbf{n}$ the outward unit normal vector, and $\mathrm{d}s$ the tangential element of the slice at Z.

Two numerical techniques, a lattice Boltzmann method (LBM) and a finite volume method (FVM), are used to solve the governing incompressible Navier–Stokes equations numerically, and a comparison is made of the calculated results. The comparison allows a deeper understanding of the effects of numerical techniques, if any, to be gained on the wake

flow, and on the structural responses and their spectral behavior. In the following, the incompressible LBM is described first and this is followed by a brief discussion of the FVM.

2.2. Lattice Boltzmann method

The Boltzmann equation describes the dynamics of nonequilibrium processes and their relaxation to thermodynamic equilibrium. It specifies the behavior of many-particle kinetic systems in terms of the basic mechanical laws governing single-particle motions at the atomic or molecular scale (Cercignani, 1988). The Boltzmann equation is formulated based on the one-body distribution function $f(\mathbf{x}, \mathbf{e}, \tilde{t})$, which is the density of molecules at position $\mathbf{x}$ and speed $\mathbf{e}$ at time $\tilde{t}$, and can be written in its dimensional form as

$$\frac{\partial f}{\partial \tilde{t}} + \mathbf{e} \cdot \nabla f = G(f, f), \tag{2}$$

where the terms on the left-hand side of Eq. (2) describe the free streaming of molecules in space, and the term $G(f,f)$ on the right-hand side of Eq. (2) represents a complicated integral operator in the velocity field expressing intermolecular interactions or collisions. Once f is known, macroscopic properties such as ρ, $\tilde{\mathbf{u}}$, and p can be obtained by integration over the molecular velocity field. The particle velocity field $\mathbf{e}$ can be discretized using a small set of vectors $\{\mathbf{e}_i\}$ such that the macroscopic conservation laws are satisfied (He and Luo, 1997a). With an assumed model for the integral collision operator G, the discretized form of Eq. (2) is called the lattice Boltzmann equation (LBE) and can be solved numerically.

The incompressible Navier–Stokes equations can be derived from the LBE through the Chapman–Enskog procedure if the density fluctuation is assumed to be negligible. However, the assumption is not always satisfied in numerical simulations using LBE. Therefore, compressibility effects in the numerical solution of the LBE might give rise to serious errors. Numerous researchers have attempted to minimize the Mach number (M) effect in the numerical solution of the LBE. Initial attempts to recover the incompressible Navier–Stokes equations were made by McNamara and Zanetti (1988) and Chen et al. (1992). More recently, He and Luo (1997b) offered an alternative to eliminate terms of order M^2 due to the density fluctuation in the existing LBM and have shown that their incompressible LBE model is also capable of recovering the incompressible Navier–Stokes equations. Since then, numerous models have been proposed for the numerical solution of the existing LBM so that the incompressible Navier–Stokes equations are recovered correctly. Among the various models put forward, the present attempt is based on that proposed by Guo et al. (2000). In the following, a brief outline of this model is described.

In order to facilitate numerical and analytical solutions of Eq. (2), the complicated nonlinear integral collision operator $G(f,f)$ is often replaced by simpler expressions to avoid mathematical difficulties (Qian et al., 1992). For example, Eq. (2) can be simplified by a BGK (Bhatnagar-Gross-Krook, 1954) collision operator and can be expressed as

$$\frac{\partial f}{\partial \tilde{t}} + \mathbf{e} \cdot \nabla f = -\frac{f - f^{\mathrm{eq}}}{\lambda}, \tag{3}$$

where λ is the relaxation time due to particle collision, and f^{eq} is the equilibrium Boltzmann–Maxwell distribution function. It can be shown that Eq. (3) can be discretized along each velocity direction $\mathbf{e}_i$ at each lattice as

$$f_i(\mathbf{x} + \mathbf{e}_i \delta\tilde{t}, \tilde{t} + \delta\tilde{t}) - f_i(\mathbf{x}, \tilde{t}) = -\frac{1}{\tau}\left[f_i(\mathbf{x}, \tilde{t}) - f_i^{\mathrm{eq}}(\mathbf{x}, \tilde{t})\right], \tag{4}$$

where $f_i(\mathbf{x}, \tilde{t})$ is the density distribution function along velocity $\mathbf{e}_i$ at the lattice position $\mathbf{x}$ and time $\tilde{t}$, $\tau = \lambda/\delta\tilde{t}$ is the relaxation parameter, and $\delta\tilde{t}$ is the time step. Hereafter, this model is designated as the lattice BGK model. The Navier–Stokes equations for incompressible gas flow can be shown to be recovered correctly by the LBM (Guo et al., 2000).

2.2.1. Solution of the lattice BGK model

The lattice BGK model can be solved as follows. In BGK formulation, the single-time relaxation equation (4) for the evolution of f_α, the distribution function for the velocity direction α, can be written as

$$f_\alpha(\mathbf{x}_i + \mathbf{e}_\alpha \Delta\tilde{t}, \tilde{t} + \Delta\tilde{t}) - f_\alpha(\mathbf{x}_i, \tilde{t}) = -\frac{1}{\tau}\left(f_\alpha(x_i, \tilde{t}) - f_\alpha^{\mathrm{eq}}(x_i, \tilde{t})\right). \tag{5}$$

This equation can be solved assuming a velocity model, which for 3-D flows could be represented by a 15-velocity (or 15-bit) lattice Boltzmann Equation (LBE) model, denoted here as D_3Q_{15}. The velocity set for

D_3Q_{15} is defined as

$$\mathbf{e} = \begin{cases} (0,0,0) & \alpha = 0;\ \text{rest particle}, \\ (\pm 1,0,0)c, (0,\pm 1,0)c, (0,0,\pm 1)c & \alpha = 1,2,\ldots,6;\ \text{group I}, \\ (\pm 1,\pm 1,\pm 1)c & \alpha = 7,8,\ldots,14;\ \text{group II}, \end{cases} \tag{6a–c}$$

where c is the lattice velocity. The solution of Eq. (5) can be achieved in two computational steps, namely,

(i) *collision step*:

$$\tilde{f}_\alpha(\mathbf{x}_i,\tilde{t}) = f_\alpha(\mathbf{x}_i,\tilde{t}) - \frac{1}{\tau}\left(f_\alpha(x_i,\tilde{t}) - f_\alpha^{\mathrm{eq}}(x_i,\tilde{t})\right), \tag{7}$$

(ii) *streaming step*:

$$f_\alpha(\mathbf{x}_i + \mathbf{e}_\alpha \Delta\tilde{t}, \tilde{t} + \Delta\tilde{t}) = \tilde{f}_\alpha(\mathbf{x}_i,\tilde{t}), \tag{8}$$

where $f_\alpha(\mathbf{x},\tilde{t})$ is the particle velocity distribution function along the αth direction at position $\mathbf{x}$ and time $\tilde{t}$; $f_\alpha^{\mathrm{eq}}(\mathbf{x},\tilde{t})$ is the equilibrium distribution function, which for the incompressible model is defined as

$$f_\alpha^{\mathrm{eq}} = \begin{cases} -4\sigma\dfrac{p}{c^2} + s_0(\mathbf{u}) & \alpha = 0, \\ \lambda\dfrac{p}{c^2} + s_\alpha(\mathbf{u}) & \alpha \text{ belongs to group I}, \\ \gamma\dfrac{p}{c^2} + s_\alpha(\mathbf{u}) & \alpha \text{ belongs to group II}, \end{cases} \tag{9a–c}$$

where

$$s_\alpha(\mathbf{u}) = w_\alpha\left[3\frac{(\mathbf{e}_\alpha \bullet \mathbf{u})}{c^2} + 4.5\frac{(\mathbf{e}_\alpha \bullet \mathbf{u})^2}{c^4} - 1.5\frac{|\mathbf{u}|^2}{c^2}\right], \tag{10}$$

σ, λ and γ are model-dependent parameters. For D_3Q_{15}, these three parameters satisfy

$$6\lambda + 8\gamma = \sigma, \tag{11a}$$

$$\lambda + 4\gamma = \frac{1}{2}, \tag{11b}$$

The weight coefficient w_α is

$$w_\alpha = \begin{cases} 2/9 & \alpha = 0, \\ 1/9 & \alpha = 1,2,\ldots,6, \\ 1/72 & \alpha = 7,8,\ldots,14, \end{cases} \tag{12a–c}$$

and the macroscopic variables are

$$p = \frac{c^2}{4\sigma}\left[\sum_{\alpha\neq 0} f + s_0(\mathbf{u})\right], \tag{13}$$

$$\mathbf{u} = \sum c\mathbf{e}_\alpha f_\alpha, \tag{14}$$

$$v = (2\tau - 1)\Delta_x c/6, \tag{15}$$

where Δ_x is the lattice length.

2.2.2. Boundary conditions

Unlike traditional computational fluid dynamics methods, the basic evolution variable in LBM is the particle distribution function f, which is usually not specified at the boundaries. Therefore, when the macroscopic variable distributions at the boundary are known, it is important to find an appropriate particle distribution such that it can meet the specified boundary condition. The nonequilibrium extrapolation treatment proposed by Guo et al. (2000) is based on the decomposition of the distribution function and still gives second-order accuracy, without having to make additional assumptions. The function $f_\alpha(\mathbf{x},\tilde{t})$ can be decomposed into an equilibrium and a

nonequilibrium part, such that

$$f_\alpha(\mathbf{x},\tilde{t}) = f_a^{\mathrm{eq}}(\mathbf{x},\tilde{t}) + f_a^{\mathrm{ne}}(\mathbf{x},\tilde{t}), \tag{16}$$

and $\tilde{f}_\alpha(\mathbf{x}_b,\tilde{t})$ at the boundary node $\mathbf{x}=\mathbf{x}_b$ is rewritten as

$$\tilde{f}_\alpha(\mathbf{x}_b,\tilde{t}) = \left(1-\frac{1}{\tau}\right) f_\alpha^{\mathrm{ne}}(\mathbf{x}_b,\tilde{t}) + f_\alpha^{\mathrm{eq}}(\mathbf{x}_b,\tilde{t}). \tag{17}$$

For the boundary node, $f_\alpha^{\mathrm{eq}}(\mathbf{x}_b,\tilde{t})$ is not known. On the other hand, the pressure is known when the pressure boundary condition is specified. Therefore, in Eq. (9), p can be taken to be the boundary pressure p_b and the velocity $\tilde{\mathbf{u}}$ can adopt the value at the neighboring interior fluid node $\tilde{\mathbf{u}}_f$. The pressure boundary condition can be similarly determined if the velocity at the boundary is specified. In the present problem, the velocity at the surface is known but not the pressure. Once the pressure on the surface is determined, the force acting on the cylinder can be calculated (Mei et al., 2002).

LBM often uses uniform regular Cartesian lattices; however, for a curved boundary, such as that encountered on a sphere and/or a cylinder, it needs special treatment (Mei et al., 2002). The curved boundary can be treated as a kind of velocity boundary condition (see Fig. 1(b)). The velocity of the object is usually known; if it is stationary, $\tilde{\mathbf{u}}_b$ equals zero. If the velocity at $\mathbf{x}_b$, $\mathbf{x}_f$ and $\mathbf{x}_{ff}$ is known, then $\tilde{\mathbf{u}}_w$ can be determined from the following extrapolations:

$$\tilde{\mathbf{u}}_w = [\tilde{\mathbf{u}}_b + (\delta-1)\tilde{\mathbf{u}}_f]/\delta \quad \text{if } \delta < 0.75, \tag{18a}$$

$$\tilde{\mathbf{u}}_w = \tilde{\mathbf{u}}_b + (\delta-1)\tilde{\mathbf{u}}_f + (1-\delta)\left[2\tilde{\mathbf{u}}_b + (\delta-1)\tilde{\mathbf{u}}_{ff}\right]/(1+\delta) \quad \text{if } \delta \geqslant 0.75. \tag{18b}$$

This kind of boundary treatment also has second-order accuracy.

2.2.3. Multi-block decomposition and local mesh refinement

For external flows, the computational domain must be large enough to allow a correct determination of the wake flow. Since the velocity gradient is very high inside the boundary layer, spatial resolution has to be high in this region. Therefore, the computational domain should be decomposed into a coarse and a fine mesh region. On the coarse-fine mesh interface, the macroscopic variables and their derivatives must be continuous. Fig. 1(c) shows the layout of the coarse and fine mesh and their interface.

From Eq. (15), if v is continuous across the fine and coarse grid, the following is obtained

$$\tau^f = \tfrac{1}{2} + m(\tau^c - \tfrac{1}{2}), \tag{19}$$

where $m = \Delta_{x,c}/\Delta_{x,f}$ is the coarse-to-fine lattice ratio, and superscripts c and f denote coarse and fine grid separately (Yu et al., 2002). Decomposing $f(\mathbf{x},\tilde{t})$ into an equilibrium and a nonequilibrium part, and maintaining continuity in the deviatoric stresses, relations between $f^c(\mathbf{x},\tilde{t})$ and $f^f(\mathbf{x},\tilde{t})$ can be deduced and they are given by

$$\begin{aligned}
\tilde{f}_\alpha^c &= f_\alpha^{\mathrm{eq},f} + \frac{\tau^c-1}{\tau^f-1}\left(\tilde{f}_\alpha^f - f_\alpha^{\mathrm{eq},f}\right),\\
\tilde{f}_\alpha^f &= f_\alpha^{\mathrm{eq},c} + \frac{\tau^f-1}{m(\tau^c-1)}\left(\tilde{f}_\alpha^c - f_\alpha^{\mathrm{eq},c}\right).
\end{aligned} \tag{20}$$

The force value can be calculated by the momentum exchange method. A nice feature of LBM is that the momentum flux tensor is available locally from its very definition. The momentum flux Φ across the plane is defined as

$$\Phi = (\tilde{f}_\alpha(\mathbf{x}_w,\tilde{t}-1) + \tilde{f}_{\bar{\alpha}}(\mathbf{x}_f,\tilde{t}))\mathbf{e}_a c, \tag{21}$$

where $\bar{\alpha}$ is the reverse direction of α.

2.3. Finite volume method

The governing equation is the 3-D unsteady incompressible Navier–Stokes equations. Written in the general convective–diffusive form, these equations in nondimensional form are

$$\frac{\partial \rho \Psi}{\partial t} + \nabla\cdot(\rho\mathbf{u}\Psi - \Gamma^\Psi \nabla\Psi) = \bar{S}^\Psi, \tag{22}$$

where $\Psi = (0,u,v,w)^{\mathrm{T}}$ is the transport quantities, $\mathbf{u}=(u,v,w)$ is the convective velocity vector, $\Gamma^\Psi = (0,1/\mathrm{Re},1/\mathrm{Re},1/\mathrm{Re})^{\mathrm{T}}$ is the diffusive coefficient, and $\bar{S}^\Psi = (0,-\partial p/\partial X,-\partial p/\partial Y,-\partial p/\partial Z)^{\mathrm{T}}$ is the source term. From this point on, only dimensionless variables are used in the equations, and the initial and boundary conditions.

The initial and boundary conditions for the flow can be summarized as

(i) at $t = 0$, the initial condition is specified as a sudden start condition,

$$u = 1, \quad v = w = 0, \quad p = 0, \tag{23a}$$

(ii) at the inlet, constant mainstream velocities with neglected boundary layer and secondary flow are specified,

$$u = 1, \quad v = w = 0, \tag{23b}$$

(iii) at the outlet, a Neumann-type boundary condition is assumed,

$$\frac{\partial \mathbf{u}}{\partial \mathrm{n}} = 0, \tag{23c}$$

(vi) at cylinder surface and ends, a no-slip condition is specified,

$$\mathbf{u} = 0, \tag{23d}$$

(v) at the transverse ends, a symmetric boundary condition is invoked,

$$\frac{\partial u}{\partial \mathrm{n}} = \frac{\partial w}{\partial \mathrm{n}} = v = 0, \tag{23e}$$

(vi) the pressure is solved using a pressure-based algorithm, while at all boundaries, the Neumann-type boundary condition is invoked for pressure and its correction p',

$$\frac{\partial p}{\partial \mathrm{n}} = 0, \quad \frac{\partial p'}{\partial \mathrm{n}} = 0. \tag{23f}$$

2.3.1. Discretization of the governing equations

A finite volume method on an unstructured mesh is used to solve Eqs. (22) and (23). A collocated mesh strategy is utilized, in which all flow variables are stored at the control volume center, or the control surface center if it lies on the boundary. Integration of Eq. (22) about an arbitrary mesh P of control volume ΔV and control surface $\mathbf{A}_f$ at time level $n+1$ yields the following semidiscretized equation,

$$\frac{\rho \Delta V}{\Delta t}\left(1.5\Psi^{n+1} - 2.0\Psi^{n} + 0.5\Psi^{n-1}\right) + \sum_{f}\left[(\rho \mathbf{u}\Psi - \Gamma^{\Psi}\nabla\Psi)\cdot \mathrm{A}\right]_{f}^{n+1} = \bar{S}^{\Psi}\Delta V, \tag{24}$$

where Δt is the time step, superscripts $n+1, n, n-1$ denote the next, present and previous time levels. The time derivative is discretized by a second-order backward implicit differencing scheme. To obtain the fully discretized form, a second-order upwind differencing scheme, a flow limiter for the convective term, and a second-order central differencing scheme for the diffusive term at both the interior and boundary surface $\mathbf{A}_f$ and pressure gradient in the source term in Eq. (24) are adopted. Recasting Eq. (24) into a standard form of finite volume formulation, the following algebraic equations relating the transport quantities Ψ at cell P with its neighboring cell nb at time level $n+1$ are obtained:

$$A_P^{\Psi}\Psi_P = \sum A_{nb}^{\Psi}\Psi_{nb} + S_T^{\Psi}, \tag{25a}$$

$$A_P^{\Psi} = \sum A_{nb}^{\Psi} + 1.5\,\frac{\rho \Delta V}{\Delta t}, \tag{25b}$$

$$S_T^{\Psi} = S_P^{\Psi} - 2.0\,\frac{\rho \Delta V}{\Delta t}\,\Psi^{n} + 0.5\,\frac{\rho \Delta V}{\Delta t}\,\Psi^{n-1}, \tag{25c}$$

where A_{nb} is the influence coefficient of neighboring cell nc on cell P, and S_P^{Ψ} is the sum of the discretized form of the source term, the higher-order convective term and the nonorthogonal diffusive term.

The velocity $\mathbf{u}_P^*$ satisfying Eq. (25) generally does not satisfy the continuity equation. A SIMPLER algorithm is applied to update the velocity $\mathbf{u}_P^*$ and the pressure p_P. The pressure correction equation for p'_P is

$$A_P^{p'}p'_P = \sum A_{nb}^{p'}p'_{nb} - \sum m_f^*, \tag{26a}$$

$$A_P^{p'} = \sum A_{nb}^{p'}, \tag{26b}$$

$$A_{nb}^{p'} = \left(\frac{\rho \Delta V}{A_P^u}\right)_f \frac{\mathbf{A}_f^2}{\sigma V}, \tag{26c}$$

$$m_f^* = \rho \mathbf{A}_f \cdot \bar{\mathbf{u}}_f^* - \left[\left(\frac{\rho \Delta V}{A_P^u}\right)_f \mathbf{A}_f \cdot (\nabla p^*)_f - \left(\frac{\rho \Delta V}{A_P^u} \nabla p^*\right)_f \cdot \mathbf{A}_f\right], \tag{26d}$$

where A_P^u is the diagonal coefficient of Eq. (24) and m_f^* is the mass flux across the control surface $\mathbf{A}_f$ between cell P and cell nb. The idea of Rhie and Chow (1983) is used in the calculation of m_f^* to prevent the well-known checker-board problem in the velocity and pressure fields. The velocity $\mathbf{u}_P^*$ and the mass flux m_f^* is updated using the pressure correction Eq. (26) and are given by

$$\mathbf{u}_P^{n+1} = \mathbf{u}_P^* - \frac{\Delta V}{A_P^u} \nabla p_P', \tag{27a}$$

$$m_f^{n+1} = m_f^* - \left(\frac{\rho \Delta V}{A_P^u}\right)_f \mathbf{A}_f \cdot (\nabla p')_f. \tag{27b}$$

In the SIMPLER algorithm, the pressure equation is the same as the pressure correction equation except m_f^*. The equations can be written as

$$A_P^{p'} p_P = \sum A_{nb}^{p'} p_{nb} - \sum m_f^{**}, \tag{28a}$$

$$m_f^{**} = \rho \mathbf{A}_f \cdot \left(\frac{\sum A_{nb}^u \mathbf{u}_{nb}^* + S_T^u}{A_P^u}\right)_f - \left[\left(\frac{\rho \Delta V}{A_P^u}\right)_f \mathbf{A}_f \cdot (\nabla p^*)_f - \left(\frac{\rho \Delta V}{A_P^u} \nabla p^*\right)_f \cdot \mathbf{A}_f\right]. \tag{28b}$$

2.3.2. Numerical solution procedure

The procedure for determining pressure and velocity at each time step can be summarized as follows:

(i) solve Eq. (25) for the intermediate velocity $\mathbf{u}_P^*$;
(ii) solve Eq. (26) and update the velocity $\mathbf{u}_P^*$ and m_f^* using Eq. (27) so that $\mathbf{u}_P^{n+1}$ and m_f^{n+1} satisfy both the continuity equation and the momentum equations;
(iii) solve Eq. (28) for the pressure p^{n+1};
(iv) repeat steps (i)–(iii) at time level $n+1$ until the sum of the absolute mass flow residual in all meshes decreases to 0.001 of the total mass flow rate across the inlet boundary, then march into the next time level.

3. Data analysis

The numerical methods allow the wake flow and the flow-induced forces to be calculated in detail. This includes the nature of the flow-induced forces, such as their stationary character or lack thereof. From all available data on the wake flow, it is most unlikely that the velocity field in the wake will become nonstationary. However, there is insufficient evidence to indicate one way or the other the stationary nature of the flow-induced forces if they are affected by the 3-D nature of the wake behind the cylinder. The forces could become 3-D and could take a long time to approach a stationary state. If the forces are indeed stationary, conventional methods such as FFT can be used to analyze the force signals, and the statistics can be calculated straightforwardly. On the other hand, if the force signals are nonstationary, a different method, such as wavelet analysis (Farge, 1992; Torrence and Combo, 1998), will have to be used to analyze the signals.

Wavelet analysis is an effective tool for analyzing localized variations of power within a time series and can be used to analyze time series that contain nonstationary power at many different frequencies (Daubechies, 1990). By decomposing a time series into time–frequency space, it is possible to determine both the dominant modes of variability and how those modes vary in time. Therefore, wavelet analysis can help to determine whether the time series reaches a stationary state or not. Wavelet analysis involves specifying a wavelet transform (WT),

$$WT(s, \bar{\tau}) = \frac{1}{\sqrt{s}} \int_{-\infty}^{\infty} w(t) \psi^* \left(\frac{t - \bar{\tau}}{s}\right) \mathrm{d}t, \tag{29}$$

where $w(t)$ is the data to be analyzed, $\psi^*(t)$ is called the mother wavelet, s is the scaling factor, and $\bar{\tau}$ is the translating factor. In the present analysis, the continuous wavelet transform (CWT) with the Morlet wavelet as the mother wavelet is used (Farge, 1992). The algorithm provided by Torrence and Combo (1998) is invoked to implement the CWT.

In the wavelet analysis, the temporal scaling factor s is used instead of the frequency commonly adopted in the conventional Fourier analysis. In order to interpret the results of the wavelet analysis in the conventional way, the scaling factor needs to be converted into the equivalent Fourier frequency. The basic idea of conversion is to substitute a single-frequency wave of a known frequency into the wavelet transform and find the temporal scaling factor at which the wavelet spectrum takes its maximum value. Repeating this procedure for a series of frequencies, the relation between the temporal scaling factor and the equivalent Fourier frequency can be established. For the Morlet wavelet, the relation is given in Torrence and Combo (1998) as $\Omega_{eq} = 1/1.03s$, where Ω_{eq} is the equivalent Fourier frequency. This Ω_{eq} is then equivalent to the frequency Ω. The vortex shedding Ω_{eq} thus deduced can be used to define an equivalent St_{eq}, and it is the same as St defined using Ω_s, i.e., $St_{eq} = St$.

In order to facilitate easy understanding and comparison with FFT calculations, the results of the wavelet analysis are presented in the form of time–frequency spectra (contour maps). Slices at selected instantaneous time are then given to demonstrate the temporal variation of the spectrum. The wavelet spectra in all these figures are dimensionless but not normalized. There is no need to normalize the spectra because only a comparison at different locations is necessary for an understanding of the spanwise variation of the forces.

4. Numerical results and discussion

Before embarking on a discussion of the simulation results, it is necessary to establish that the solutions obtained from the FVM and the LBM are convergent and are essentially grid independent. Common to both methods are the inlet condition and the upstream distance. For the present calculations, the inlet is chosen at $X = -10$ and an impulsively started initial condition is applied. The same initial condition is imposed on the FVM and LBM. However, the computational domain for the two methods is slightly different.

For the LBM the domain is chosen to be $50 \times 16 \times 16$. In order to resolve the flow around the cylinder more accurately, a refined grid with a domain size given by $7 \times 4 \times 16$ is placed around the cylinder with the upstream boundary located at $X = -1.5$. The coarse grid is defined by $\Delta_{x,c} = D/8$ and the fine grid is defined in the present calculations as $\Delta_{x,f} = D/N$, where N is any multiple of 8. Two different fine grids have been examined: one given by $N = 24$ and another by $N = 32$, i.e., $m = 3$ and 4, respectively. With these grids, there are 48 and 64 lattices around the cylinder, respectively. The calculated mean drag coefficient $\bar{C}_D$ and the root-mean-square lift coefficient C'_L deduced from the calculations at the same t using these two different grids do not differ by more than 1%. In view of this, the following calculations using the LBM are carried out with $m = 3$.

For the FVM, the computational domain is $35 \times 16 \times 16$. Two different mesh sizes and distributions were investigated in the FVM calculations. One has 160 nodes around the cylinder circumference with 64 layers along the cylinder span, while another has 200 nodes and 80 layers. The calculated $\bar{C}_D$ and C'_L are deduced from these two sets of simulations. It is found that the difference between these calculated values is less than 1.2% of each other at the same t. Therefore, these solutions can be considered to be convergent and grid independent for both the FVM and LBM simulations.

The objective of the present study is to investigate the effect of a 3-D wake flow on the flow-induced forces along the span of a long slender cylinder. A secondary objective is to further investigate the consistency of the calculated C'_L for 3-D cylinders in a cross flow at $Re = 100$. In order to achieve these objectives, it is necessary to first demonstrate that the present numerical methods could replicate the 2-D results reported in Norberg (2003) and that the wake behind the long slender cylinder at $Re = 100$ is indeed 3-D. Once the reliability of the numerical methods is established, the results of either the LBM or the FVM could be used to analyze the effects of the 3-D wake on the flow-induced forces. In the following discussion, results of the calculated 2-D case are presented first. This is followed by an examination of the wake flow and the characteristics of the flow-induced forces. Once the character of the forces has been established, a proper technique could be used to analyze the forces distribution along the span and to determine their spectral contents and spanwise correlations. Finally, an attempt is made to evaluate the effect of a on the calculated flow-induced forces and wake flow, including their 3-D behavior or lack thereof.

4.1. 2-D calculations

The 2-D calculations were carried out around a circle, i.e., assuming the cylinder span to be infinite and the flow to be homogeneous along the cylinder axis. Only the calculated $\bar{C}_D$, C'_D and C'_L are reported in Table 1 together with 2-D

Table 1
Comparison of calculated and measured $\bar{C}_D$, C'_D and C'_L at Re = 100

	Re	Calculation/measurements	L/D	$\bar{C}_D$	C'_D	C'_L
Schlichting (1955)	100			~ 1.70		
Norberg (2003)	100					0.14–0.35
He and Doolen (1997)	50–150	2D calculations				0.23
Present FVM	100			1.78	0.0079	0.327
Present LBM				1.27	0.003	0.24
Norberg (1994)	100		16			0.11–0.52
Zhang and Dalton (1998)	100		11	1.32[a]		0.23[a]
Zhang and Dalton (1998)	200		15			0.43[a]
Persillon and Braza (1998)	100	3-D calculations	∞	1.24[a]		
Mittal (2001)	100		16	1.34[b]		0.033[b]
Present FVM	100		16	1.56b	0.0012	0.035[b]
Present LBM			16	1.31[b]	0.0013	0.043[b]
Present FVM			16	1.60[c]	0.0016	0.074[c]
PresentLBM			16	1.34[c]	0.0048	0.074[c]
Tanida et al. (1973)	60–110		10			0.03–0.09[d]
Tanida et al. (1973)	100		10	1.26		
Tritton (1959)	105	3-Dmeasurements	187.5	1.25		
Khalak and Williamson (1996)	200–1300		10			0.03–0.30[d]
Jordan and Fromm (1972)	100			1.29		
Roshko (1954)	100			1.29		

[a]With periodic boundary condition at cylinder ends.
[b]Value at mid-plane and with end walls.
[c]Spanwise average over whole span.
[d]Spanwise average over active span.

data collected from Schlichting (1955), He and Doolen (1997), and Norberg (2003). For both FVM and LBM, the calculated values of St are 0.166 and 0.161, respectively, and $\bar{C}_L$ is essentially zero; the numerical calculation error in $\bar{C}_L$ amounts to four orders of magnitude less than $\bar{C}_D$. The corresponding St reported by Norberg (2003) is 0.16–0.17, thus the present calculated St falls within this range. It can be seen that both LBM and FVM give a consistent prediction of St and the calculated C'_L compares well with those reported in the literature. The predictions of FVM tend to be on the high side; however, they are still within the range of reported results for a 2-D cylinder. The difference between the FVM and LBM calculated $\bar{C}_D$ and C'_L are 39% and 36%, respectively. However, the FVM calculated $\bar{C}_D$ is only in line with previous experimental data at Re = 100 (Schlichting, 1955), but not so with more recent measurements (Table 1). On the other hand, the FVM and LBM calculated C'_L are consistent with the data collected byNorberg (2003) and with that obtained by He and Doolen (1997) using a LBM technique.

The near-wake velocity vector and vorticity component ω_z plots are given in Figs. 2(a) and 3(a), respectively. The plots are derived from FVM calculations and are taken at a dimensionless time $t = \tilde{t}D/U_\infty = 800$, where the lift signal shows stationary behavior. Similar plots can be obtained from the LBM results. The velocity vector plot in the near wake ($-2 < X < 5$) substantiates the ω_z distribution, which is given in the range $-5 < X < 22$. Clearly, alternating vortex shedding with a 2S pattern is replicated. These results are consistent with those reported in the literature. Therefore, both LBM and FVM results are reliable to within the range reported by other investigators and the mesh size and mesh density are acceptable.

4.2. 3-D wake characteristics

It has been known that vortex shedding from nominally 2-D bluff body exhibits certain 3-D characteristics. The simple way to identify these 3-D characteristics is through numerical flow visualization. This can be accomplished by visualizing the velocity vector and ω_z plots in the near wake of a long slender cylinder in a cross flow. The velocity vector plots at three different Z locations ($Z = 0$ and ± 4) are shown in Figs. 2(b)–(d), while the corresponding ω_z plots

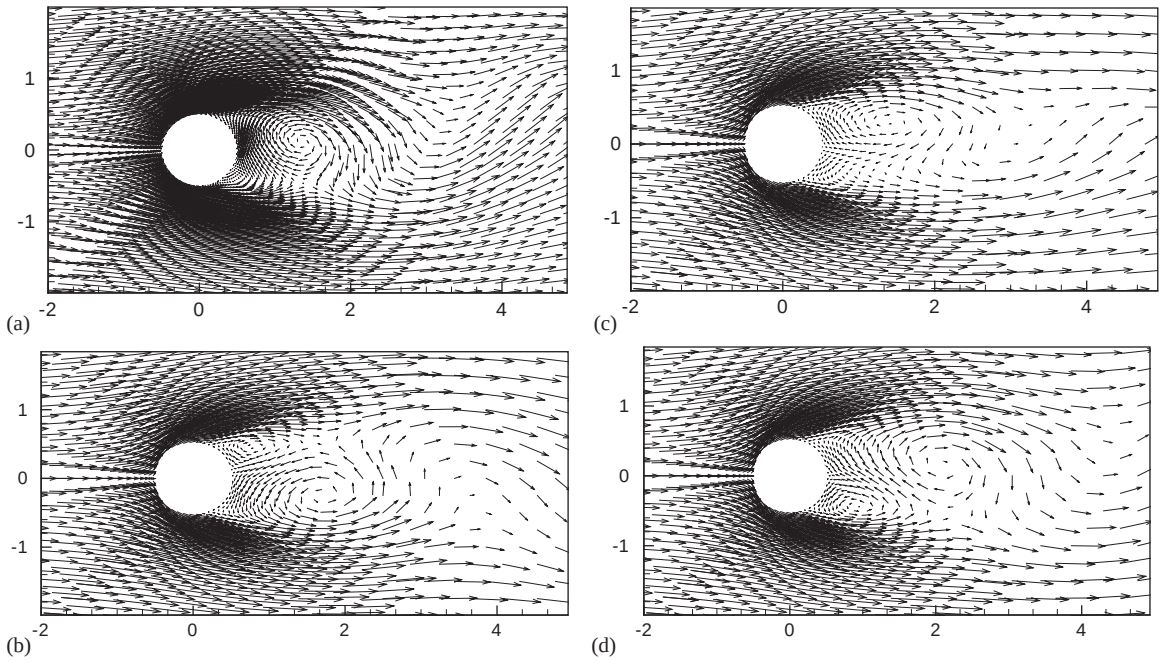

Fig. 2. Near-wake velocity distribution for flow around 2-D and 3-D cylinder at stationary state: (a) 2-D case; (b) $Z = 4$ of 3-D case; (c) $Z = 0$ of 3-D case; (d) $Z = -4$ of 3-D case.

are given in Figs. 3(b)–(d). The range shown for the velocity vector plots is $-2 < X < 5$ and the corresponding range for ω_z is $-5 < X < 22$. The velocity vector plots are used to substantiate the interpreted 3-D behavior of the ω_z distributions. The contour plot of ω_z in the X–Z plane at $Y = 0$ is displayed in Fig. 4.

It is clear from the velocity vector plots that the near wake velocity distribution at $Z = 0$ for the long slender cylinder (Fig. 2(c)) is different from that shown for the 2-D case (Fig. 2(a)). Two elongated vortices shed at about the same time are discernible in Fig. 2(c) while alternating shedding is indicated in Fig. 2(a). This observation is consistent with the ω_z plots shown in Fig. 3. The velocity vector plot of Fig. 2(a) suggests that, in the near-wake region ($-2 < X < 5$), the vortex shedding pattern is such that, in one cycle, two vortices are released, one from the bottom and another from the top. In other words, a 2S shedding pattern is established (see Fig. 3(a)). The same is not true for the long slender cylinder (Fig. 3(c)). However, this behavior changes back to alternate shedding away from the $Z = 0$ plane, as can be seen from the velocity vector plots shown in Figs. 2(b) and (d). For example, the vortices are shed alternately at $Z = \pm 4$ but they have different phase; at $Z = 4$, the large vortex is shed from the bottom side (Fig. 2(b)), while the reverse is true at $Z = -4$ (Fig. 2(d)). More about this antiphase behavior can be inferred from the ω_z plots (Fig. 3). This phase variation is evidence of the lack of similarity in the near wake velocity vector plot along the span and lends credence to the interpretation that the wake flow is indeed 3-D. This finding is consistent with the work of Roshko (1954) who showed that vortices shed from a circular cylinder in the Re range 50–150 are not necessarily 2-D, but that a periodic phase variation may exist parallel to the cylinder axis.

Fig. 3 shows the ω_z distribution for the 2-D case and in different Z-planes for the long slender cylinder. For the 2-D case, a 2S type vortex shedding is observed (Fig. 3(a)). In the $Z = 0$ plane of the long slender cylinder, a 2P type vortex shedding is displayed (Fig. 3(c)). This 2P type vortex shedding is similar to the one identified by Williamson and Roshko (1988) for a cylinder under forced oscillation. In the present case, the formation of the 2P type vortex shedding at the $Z = 0$ plane could be due to oblique shedding, which gives rise to an antiphase vortex shedding along the span (see Section 4.5 for more details of the antiphase behavior of the C_L contours behind the cylinder). The pairing occurs downstream at about $X = 7$ and is not visible in the velocity vector plots. At $Z = \pm 4$, the vortex shedding pattern is such that in one cycle two vortices are released, one from the bottom and another from the top. However, the two shed vortices quickly organize themselves into single vortices like those shown for the 2-D case (Figs. 3(b) and (d)). This shedding behavior resembles the 2S type. Unlike the 2-D case, the shedding along the span is antiphase though. For example, at $Z = 4$, the large vortex is shed from the top (Fig. 3(b)), while the reverse is true at $Z = -4$ (Fig. 3(d)), hence

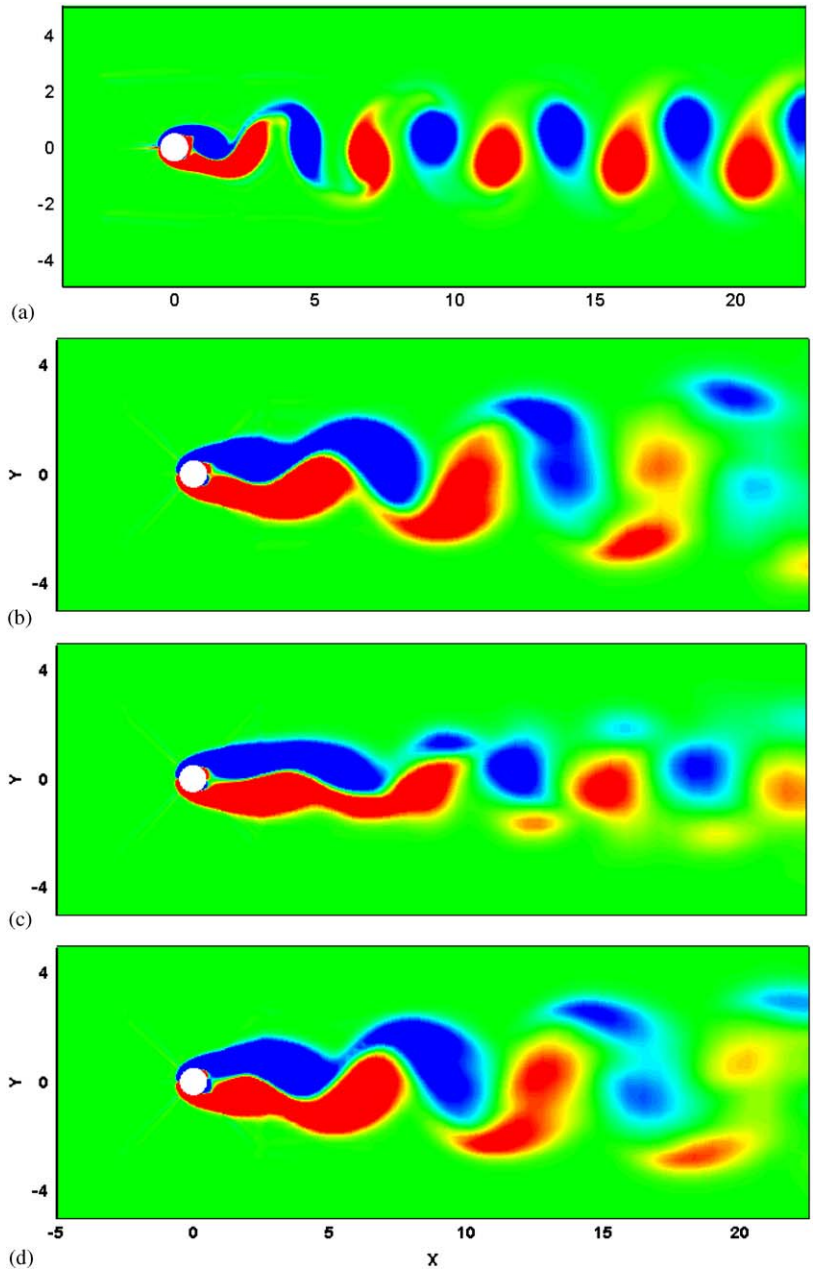

Fig. 3. Near-wake vorticity component ω_z distribution for flow around 2-D and 3-D cylinder at stationary state: (a) 2-D case; (b) $Z = 4$ of 3-D case; (c) $Z = 0$ of 3-D case; (d) $Z = -4$ of 3-D case.

the vortex shedding is antiphase. In general, the vortex shed is quite strong immediately behind the cylinder at $Z = \pm 4$; but the vortex is split into two smaller vortices further downstream (Figs. 3(b) and (d)). These ω_z distributions are quite different from those shown in Fig. 3(a) and further substantiate the 3-D character of the wake flow.

Other key 3-D features of the wake of a nominally 2-D body are oblique shedding and vortex dislocation. The ω_z distributions at $t = 600$ and 900 in the X–Z plane at $Y = 0$ are shown in Fig. 4. The behavior of the lift signal is different at these two different times. As can be seen from Fig. 6, the lift signal appears to be in a quasistationary/transitional state at $t = 600$ and in a stationary state at $t = 900$. It can be seen that parallel vortex shedding is dominant

along the span at $t = 600$, while oblique vortex shedding along the span is distinctly visible at $t = 900$. At this time, vortex shedding seems antisymmetric about the $Z = 0$ plane, thus indicating that out-of-phase vortex shedding could be a consequence of the oblique shedding or *vice versa*. Also, the oblique shedding angle appears to be almost constant along the entire span.

Irrespective of whether the vortex shedding is parallel or oblique, there is only one vortex cell within the spanwise region for both plots shown in Fig. 4, thus suggesting that the shedding frequency Ω_s is the same along the entire span. Indeed, the FVM and LBM calculated values of St are constant along the span and they are 0.142 and 0.145, respectively, (Fig. 5). These values of St agree fairly well with 0.145 calculated by Mittal (2001) and 0.140 measured by Norberg (1994). The St value obtained is not a good indication of whether the vortex shedding and/or the wake flow is 3-D in nature. At this point, it is appropriate to point out that, in the past, most calculations were seldom carried out to $t = 900$ and beyond. As a result, they failed to observe the oblique vortex shedding reported in the present calculation. This could be one of the reasons why the conclusion was drawn that the wake flow was approximately 2-D because vortex shedding behavior was essentially the same along the cylinder span. However, the oblique shedding, plus other results presented above, show that the wake flow behind a nominally 2-D cylinder, in this case a long slender cylinder, is essentially 3-D and there is no symmetry about the $Z = 0$ plane. In view of this, the presently investigated long slender cylinder case is labeled the 3-D case in contrast to the 2-D case.

4.3. Unsteady flow-induced forces

For most 3-D calculations, periodic boundary conditions are invoked at both ends of the cylinder. The period assumed is usually not more than several π (Evangelinos and Karniadakis, 1999). Due to the large storage requirements for 3-D calculations, it is the normal practice to terminate the calculation after the C_L time series reaches a "stationary state". The stationary behavior of the C_D time series is seldom checked. In fact, it is tacitly assumed that, once the C_L time series becomes stationary, the C_D time series will also be stationary. Subsequently, calculations were carried out to around $t = 300$ where the C_L time series has achieved a stationary state. This assumption may not be valid because cross-talk between the X and Y directions could affect the behavior of the C_L and C_D time series. It is also misleading because most calculations have not been carried out far enough in time to show that the stationary state achieved is truly stationary for both the C_L and C_D time series.

A cylinder with two end-walls in a cross-flow is simulated in the present study. The simulation covers the entire span of the cylinder and the calculation is carried out to a very large value of t. In the process of performing the calculations, it has been found that the time series cannot reach a "stationary state" until it is great enough to capture the phase transition (see Section 4.5). The time required is different for the FVM and the LBM, and even after a "stationary state" has been reached for the C_L time series, there is no guarantee that similar behavior can be established for the C_D time series at the same value of t. In view of the fact that the C_D time series takes a long time to settle down and may or may not become "stationary", the calculations were carried out to $t = 600$ for the LBM and to $t = 900$ for the FVM.

The time series plots of C_L and C_D at $Z = 0$ derived from FVM and LBM calculations are shown in Figs. 6 and 7, respectively. For the FVM calculation, the C_L time series displays a constant amplitude behavior when $t > 200$, and this behavior extends to about $t \sim 500$. This t range more than covers the normal period reported in the literature. As the calculation continues, the amplitude of the C_L time series begins to decrease at $t \sim 600$, and after a transition period it reaches a new "stationary state" at $t \sim 700$, and this new " stationary state" continues to $t = 900$ where the calculation is terminated (Fig. 6(a)). Due to the variation of the C_L time series within the range $200 < t < 900$, there is no guarantee that this new "stationary state" would represent a true stationary state for C_L. In order to explore this conjecture, the calculations were carried out to $t = 1500$. No further variation was observed and the C_L signal was found to continue its behavior as shown in Fig. 6(a) for $t > 800$. The initial "stationary state" behavior could shed light on the wide variations noted in the reported C'_L in the literature. It appears that the time of termination of the calculations has a significant impact on the calculated C'_L. A more detailed analysis of this behavior will be carried out in the analysis of the characteristics of the flow-induced forces in the next section. Furthermore, it will be shown that the reduction in amplitude of the C_L time series could be attributed to a vortex-shedding phase change. The amplitude of the C_L time series decreases continuously after $t \sim 150$ and the decrease continues to about $t = 400$ (Fig. 6(b)) for the LBM result. Thereafter, the C_L time series reaches a "stationary state" and this continues to $t = 1500$ without any more variation in its amplitude, just like the result given by FVM.

Corresponding plots of the C_D time series are shown in Fig. 7; the FVM result is plotted in Fig. 7(a) and the LBM calculation in Fig. 7(b). The FVM calculated C_D follows its C_L counterpart closely with a seemingly "stationary state" in the range $300 < t < 600$ and another stationary state beyond $t > 800$ (Fig. 7(a)). The LBM calculated C_D, however,

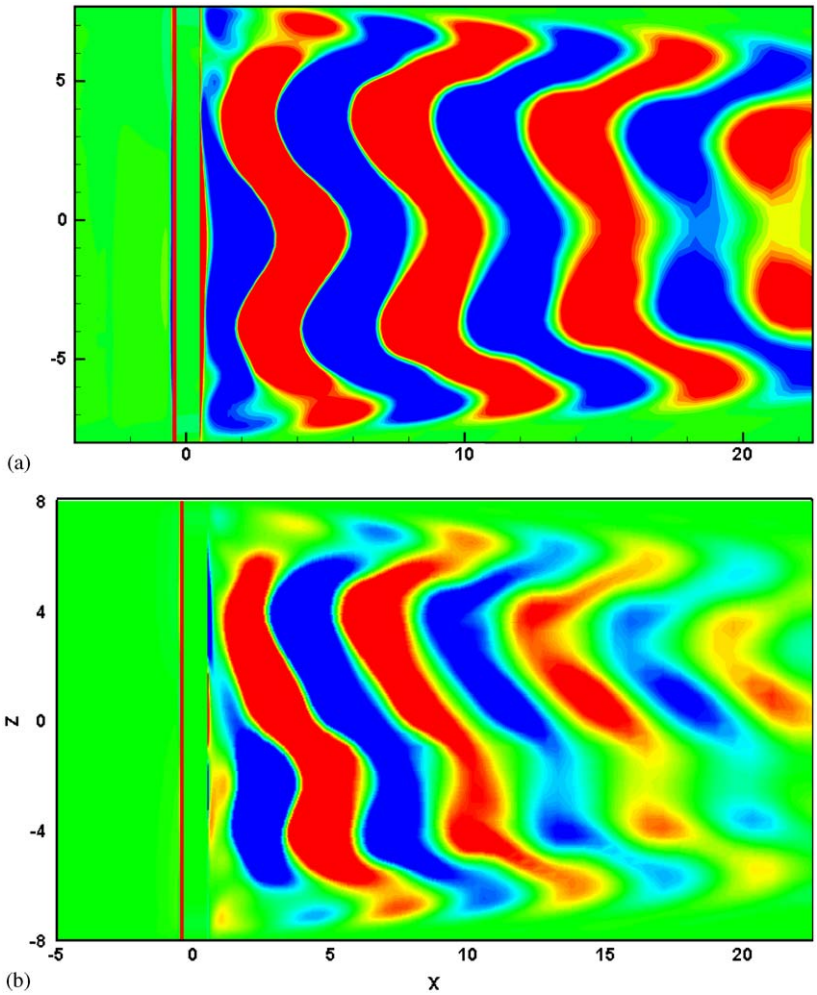

Fig. 4. Vorticity component ω_z distribution in the $Y = 0$ plane at two different t: (a) $t = 600$ in the quasi-stationary state, parallel shedding; (b) t = 900 in the stationary state, oblique shedding.

behaves differently from its C_L counterpart (Fig. 7(b)). A slight decrease followed by a slight increase behavior in the range $150 < t < 450$ is discernible. Thereafter, the C_D time series appears to reach a stationary state beyond $t = 450$ and the mean value seems to be fairly constant. Examining the data up to $t = 1500$ fails to reveal a different behavior. This raises a question concerning the true stationary behavior of the flow-induced forces. In view of this, CWT is used to analyze the spectral characteristics of both the C_L and C_D time series.

4.4. *Spectra of the flow-induced forces*

The spectra of C_L and C_D calculated using the CWT technique are shown in Figs. 8–11. Time series data at $Z = 0$ and ± 4 is chosen from the LBM results in the range $500 < t < 610$ where the C_L signal appears to be stationary while the corresponding C_D time series might not be stationary. The C_L and C_D spectra at $Z = 0$ and ± 4 are plotted in Figs. 8 and 9, respectively, with St ($= \mathrm{St_{eq}}$) versus t. These figures represents a series of power spectra density of C_L and C_D plotted on the t-axis. Therefore, at a fixed t, the plot becomes the power spectral density against St. This is why the ordinate is St and the vortex shedding frequency Ω_s can be easily determined from the plots. It is obvious that the C_L time series is stationary, because the power spectral density plot does not change with time. Variation with Z is

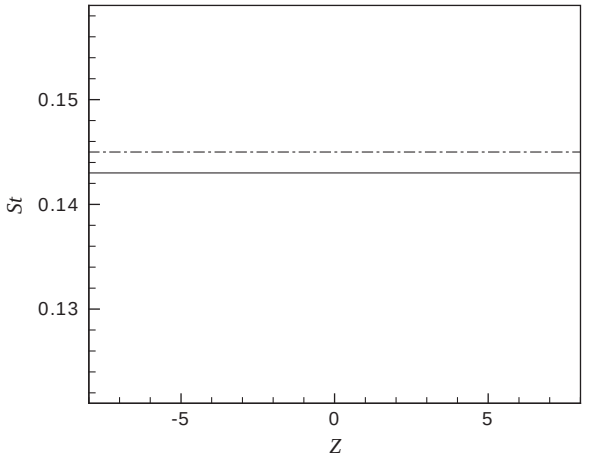

Fig. 5. Distribution of St along the span: – – ––, FVM; – – · – –, LBM.

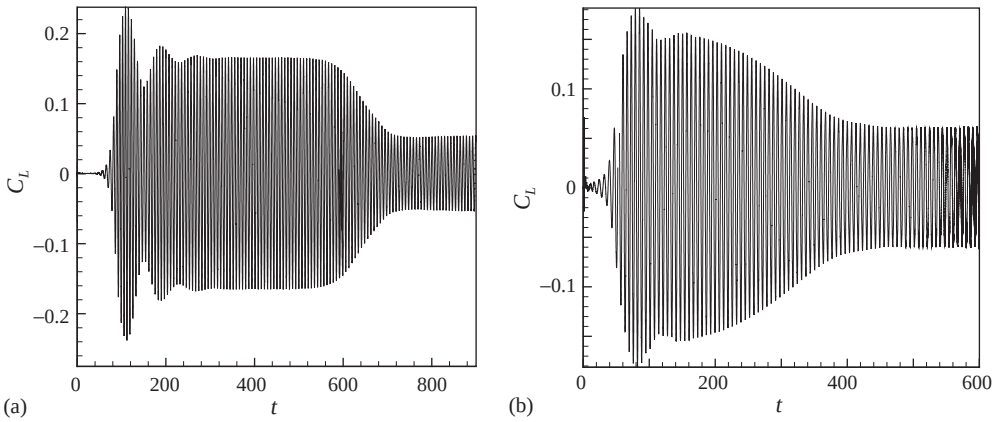

Fig. 6. C_L time series at Re = 100 and $a = 16$: (a) FVM; (b) LBM.

illustrated by plotting the spectra at a particular t such as shown in Fig. 10. It can be seen that there is no symmetry about $Z = 0$ and clearly shows that C_L varies along the span. The dominant frequency is Ω_s and this is recovered correctly from the CWT calculated spectra. From Fig. 8, it can be determined that St (= $\mathrm{St_{eq}}$) = 0.145. Thus determined, St is the same as that deduced from a straightforward application of FFT to analyze the C_L time series.

The C_D spectra are shown in Fig. 9 and they reveal variations with t and Z. These variations can be further illustrated by comparing the spectra at different t and this is carried out in Fig. 11, where the spectra at $Z = 0$ and ± 4 for two different t are shown. Again, the spectra show that C_D like C_L varies along the span. In addition, the spectra of C_D evaluated at $t = 560$ and 562 show differences for all three Z locations. This is evidence that true stationarity has not been reached, at least not at $t = 562$. The dominant frequency of the C_D signal is $2\Omega_s$ and this is correctly recovered at $Z = 0$ and ± 4. Besides $2\Omega_s$, higher harmonics, such as $3\Omega_s$ and $4\Omega_s$, are also visible in the spectral plots. The spectral plots in the $Z = \pm 4$ planes show a higher energy content than those at $Z = 0$. This variation seems to indicate that, even though the shedding frequency is stationary, the drag time series itself might not be stationary. From these spectral plots, it could be inferred that the cross-talk between the lift and drag coefficient may not be very pronounced because higher harmonics are not noticeable in the C_L spectra. In spite of this, a one-degree-of-freedom model should not be invoked in the analysis of a freely vibrating beam excited by flow-induced forces (Chilukuri, 1987). More will be said about the lack of stationary behavior in C_D in the statistical analysis of the C_L and C_D time series.

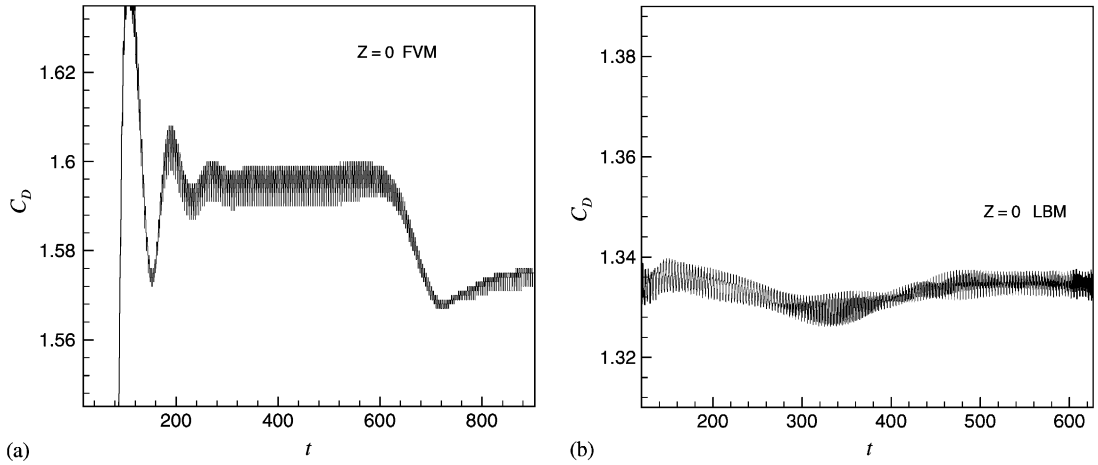

Fig. 7. C_D time series at Re = 100 and $a = 16$: (a) FVM; (b) LBM.

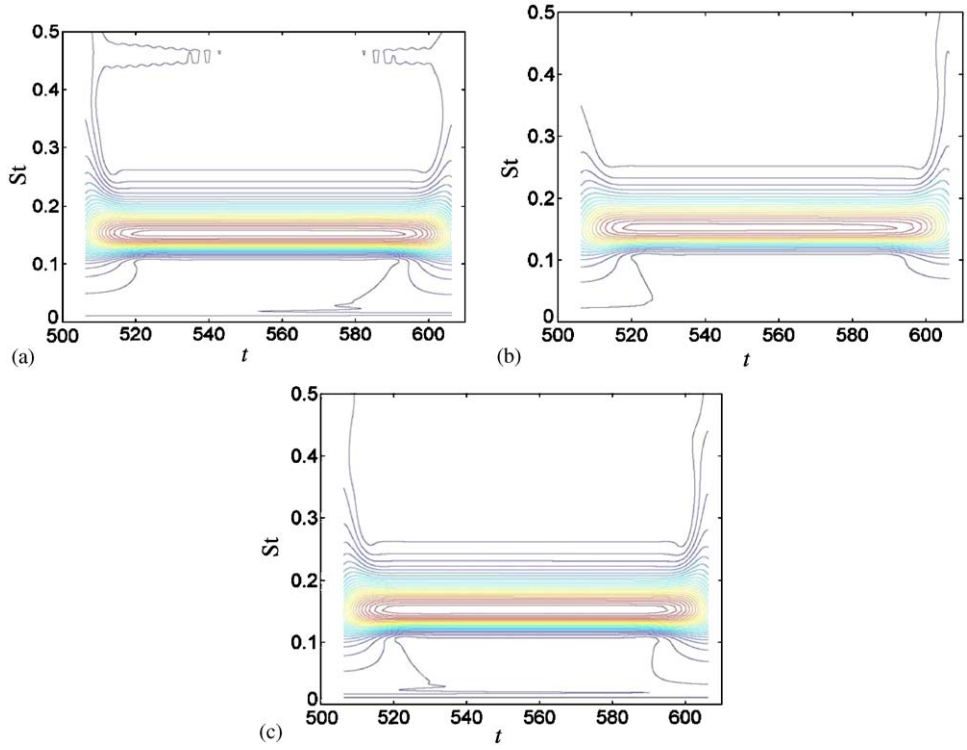

Fig. 8. Wavelet analysis of stationary C_L time series calculated by LBM at (a) $Z = -4$, (b) $Z = 0$, and (c) $Z = 4$. The curves denote the power spectral energy of C_L in the St–t map.

4.5. Phase shift of the lift force along the span

Experiments have shown that, instantaneously, there are substantial variations in the phase of vortex shedding over a spanwise distance (Roshko, 1954; Szepessy, 1994). In fact, the experimental studies of Roshko (1954) revealed that periodic phase variation may exist parallel to the cylinder axis. Time series and the vorticity distribution may not show the phase variation clearly; therefore, a C_L contour over a $t \sim Z$ domain could help to further understand the phase change evolution of C_L. The FVM calculated results at quasi-stationary, transition and stationary states are used to

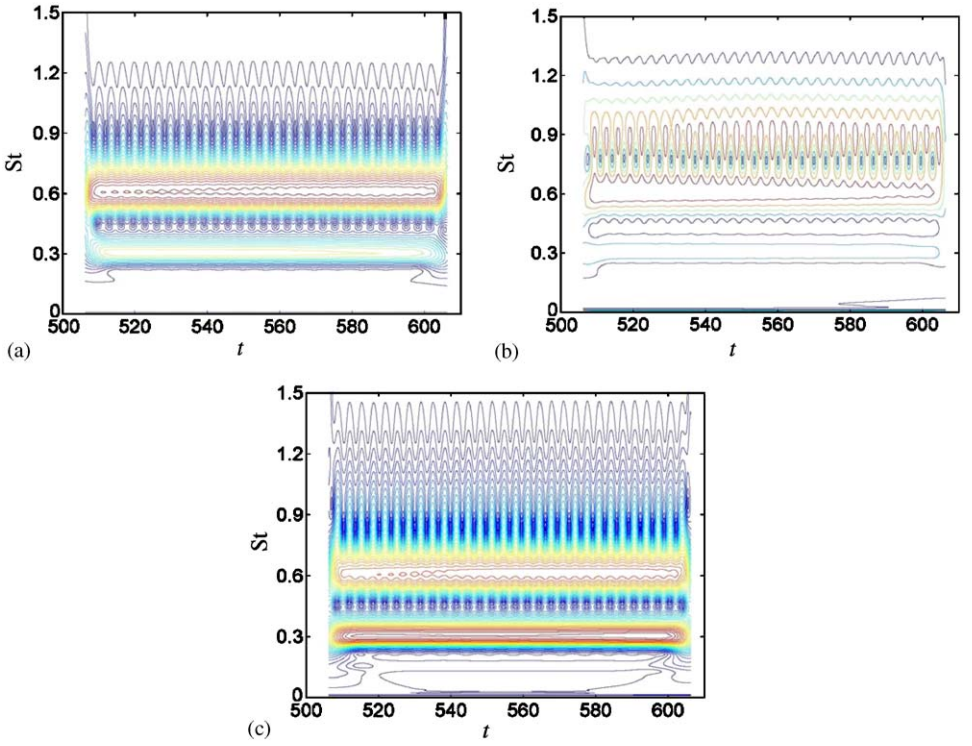

Fig. 9. Wavelet analysis of stationary C_D time series calculated by LBM at (a) $Z = -4$; (b) $Z = 0$; and (c) $Z = 4$. The curves denote the power spectral energy of C_D in the St–t map.

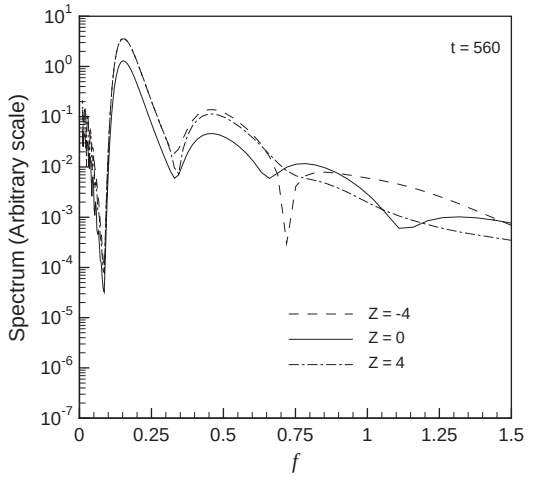

Fig. 10. Spectral analysis of C_L at $t = 560$.

construct the contours in the $t \sim Z$ domain and are shown in Figs. 12(a)–(c), respectively. Similar results are obtained using LBM-derived data. However, the two results only differ quantitatively in the calculated C'_L but not in the trend shown in Fig. 12. The C_L contours at $t = 300$–350, which correspond to the quasi-stationary state, are displayed in Fig. 12(a). These C_L contours seems to be symmetric about the cylinder midspan. They show that, along the span, the C_L distribution is essentially flat in the central region, the vortex shedding frequency does not vary, and vortex shedding is nearly in-phase even though a slight phase difference exists along the span. On close examination, it can be seen that

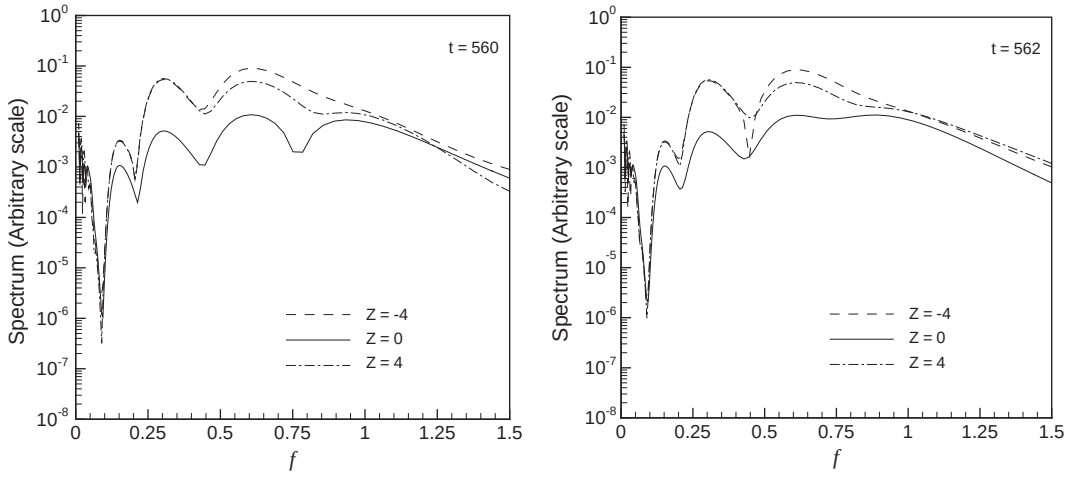

Fig. 11. Spectral analysis of C_D at $t = 560$ and 562.

the C_L contours are not exactly stationary, because the C_L cell is still changing with time. In the transition state, $t = 630$–730 as shown in Fig. 12(b), the C_L contours are no longer symmetric about the cylinder midspan, and the vortex shedding phase difference becomes larger and larger along the span with increasing time. Two C_L cells are formed behind the cylinder, but the shedding frequency is still the same along the span. As t increases to 800–850, the C_L contours become asymmetric about $Z = 0$ as shown in Fig. 12(c), thus indicating an antiphase vortex shedding along the span. As observed in Section 4.2, this out-of-phase vortex shedding could be a consequence of the oblique shedding(Fig. 4(b)). Past results failed to observe this behavior because the calculations were seldom carried out to $t = 900$ and beyond. Another reason for the antiphase vortex shedding could be due to the existence of a valley in the spanwise distribution of C'_L whose behavior is discussed in detail in Section 4.6. The C_L contours are stationary because there is no discernible change with time up to t = 1500. Again, the shedding frequency appears to be the same along the span (Fig. 5). This sequence of events shows that a phase transition has taken place in the approach to a stationary state.

4.6. Force variation along cylinder span

In order to further pursue the behavior of the C_L and C_D time series, the variation of their mean and r.m.s. values with Z and t are analyzed. To this end, two methods are used to calculate the statistics; one is the conventional method of straightforwardly calculating the first and second moment of the time series over a long time period; another is to use the running-time-average method (RTA) which is consistent with the spirit of CWT to determine the mean and r.m.s. values. In the latter method, a slice of range $2T$ centered round an instantaneous time t is chosen for the determination of the mean and r.m.s. values at t. This slice is then moved along the time axis to determine the variation of the mean and r.m.s. values as a function of t. If the time series is indeed stationary, the mean and r.m.s. values thus determined will remain constant with respect to t, provided $2T$ is much larger than the period of the stationary signal. All signals used to determine the mean and r.m.s. values are taken from the time series at $t > 400$ for LBM and at $t > 700$ for FVM.

The time variations of $\bar{C}_D$ and C'_D determined using RTA are shown with the results from FVM in Fig. 13 and the corresponding LBM calculations in Fig. 14. In the process of deducing these values, the optimum $2T$ is found to be 60. Consequently, the results reported in Figs. 13 and 14 specified $2T = 60$. In each panel, the time variations of $\bar{C}_D$ and C'_D for several Z locations are shown. There is no need to show the C'_L results because, in the previous section, the C_L time series has been demonstrated to be stationary irrespective of whether it is derived from the FVM or the LBM simulations. From these plots, it can be seen that the FVM calculated $\bar{C}_D$ and C'_D are stationary because there is essentially no variations within the time period covered in Fig. 13. This is not quite true for the plots shown in Fig. 14 based on the LBM result. The time period covered is much longer in Fig. 14. Even though $\bar{C}_D$ is stationary (Fig. 14(a)), C'_D does not appear to be stationary because its value undergoes variation with t (Fig. 14(b)). The variation differs depending on Z; it is greatest for $Z = 6$ and least for $Z = 0$ in the time period from 400 to ~ 600. Taking the period from 700 to 900, the variation is essentially the same for all four Z locations and it is milder than in the earlier time

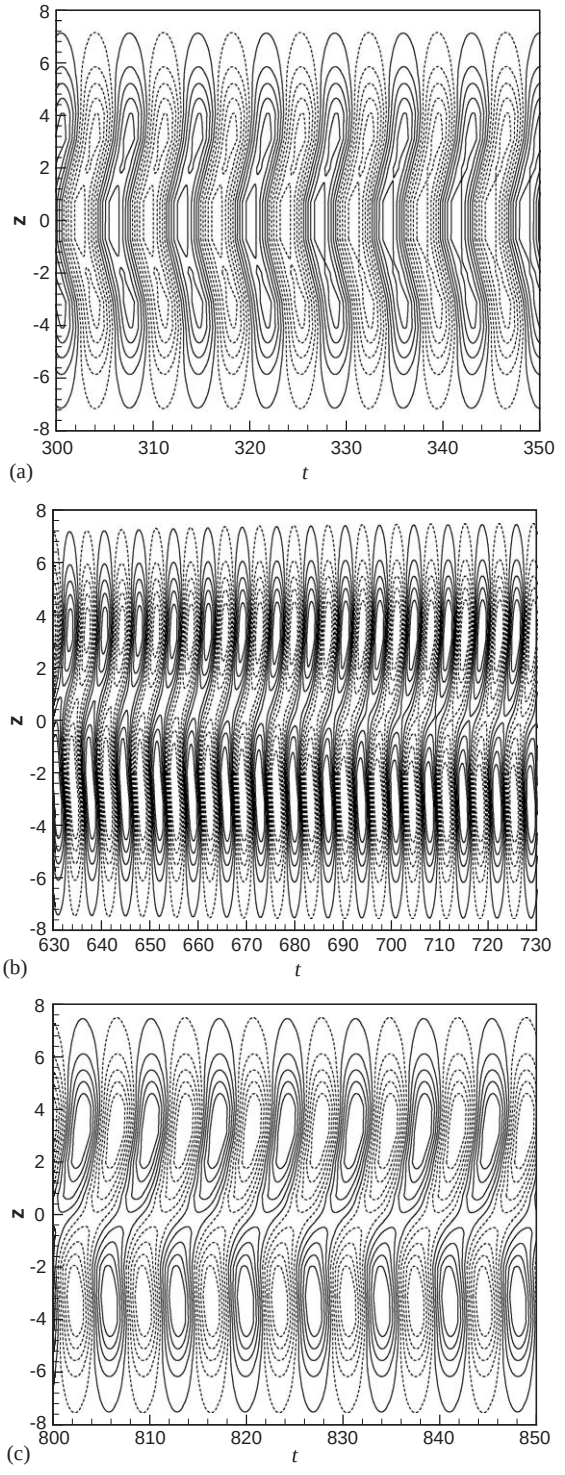

Fig. 12. C_L contours in t–Z plane: (a) quasi-stationary state; (b) transition state; (c) stationary state.

period. Even then, C'_D shows a discernible variation with time. This C'_D dependence on t lends credence to the conclusion that the LBM calculated C_D signal is not quite stationary, even though the calculated $\bar{C}_D$ has reached a stationary state at $t > 400$.

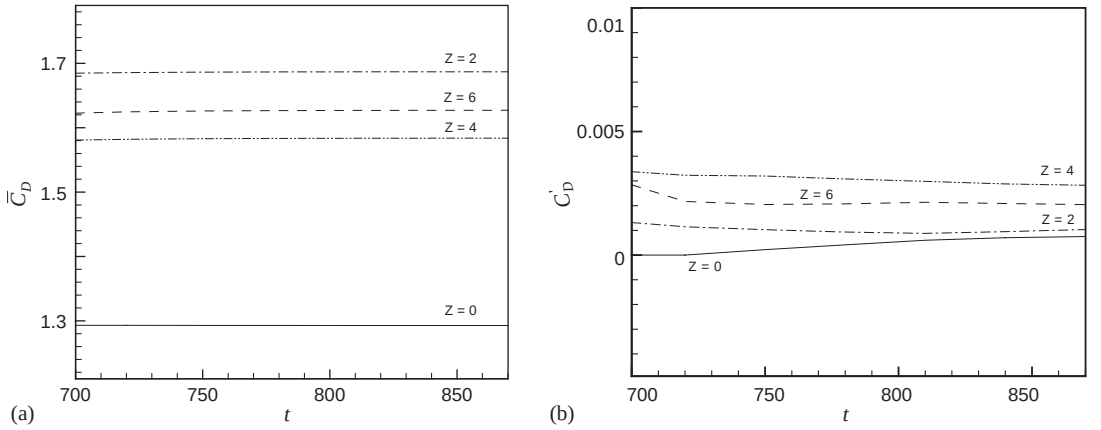

Fig. 13. Variation of FVM-calculated $\bar{C}_D$ and C'_D with t for several different Z: (a) $\bar{C}_D$; (b) C'_D.

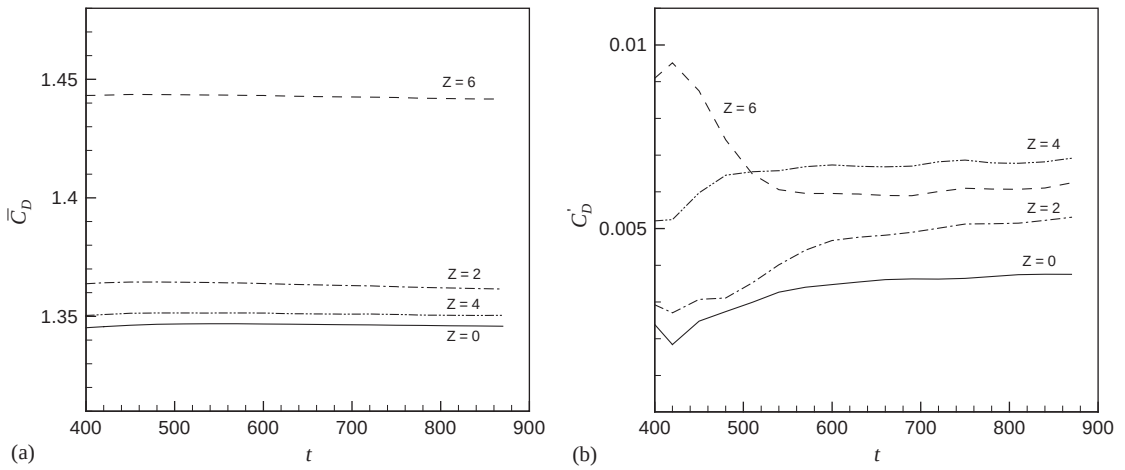

Fig. 14. Variation of LBM-calculated $\bar{C}_D$ and C'_D with t for several different Z: (a) $\bar{C}_D$; (b) C'_D.

Since the FVM calculated C_D and C_L are stationary, the straightforward time averaging method can be used to calculate $\bar{C}_D$, C'_D, $\bar{C}_L$, and C'_L; these results are reported in Table 1 and plotted in Figs. 15 and 16. Even though the LBM calculated C_D has not yet approach a stationary state, an initial comparison is attempted by calculating $\bar{C}_D$, C'_D, $\bar{C}_L$ and C'_L using the straightforward time averaging method and the results are also listed in Table 1 and plotted in Fig. 15. Two different sets of values are reported in Table 1; one lists the calculated values at the midspan of the cylinder, another lists the average over the entire span L of the cylinder. The distributions of $\bar{C}_L$ and $\bar{C}_D$, and C'_L and C'_D along the cylinder span are shown in Figs. 15 and 16, respectively. In these figures, the time averaging distributions and the RTA calculations at $t = 800$ for the FVM and at $t = 450$ for the LBM are also shown. If the time series is truly stationary, both the time averaging values and the RTA calculations should agree with each other. The degree of agreement is an indication of the stationary nature of the C_D signal.

For a cylinder in a uniform cross-flow, $\bar{C}_L$ should be identically zero. The magnitude of $\bar{C}_L$—an average of ~ 0.00045 for the FVM and ~ 0.00060 for the LBM—and its variation along Z is an indication of the calculation error of the numerical techniques (Fig. 15(a)). These values are at least two to three orders of magnitude less than the calculated C'_L (Fig. 16(a)) and three orders of magnitude less than $\bar{C}_D$. The time average values are not in agreement with the RTA calculations; however, the maximum discrepancy is of the order of 0.0002 for the LBM and 0.0003 for the FVM. These discrepancies are smaller than the calculation error of the two methods. Within the calculation error margin, the two methods could be considered to replicate $\bar{C}_L$ correctly, i.e., essentially zero $\bar{C}_L$ along the span.

An inspection of Fig. 15(b) shows a significant variation of $\bar{C}_D$ along the span. Overall, the FVM calculation is higher than the LBM result, consistent with the 2-D calculations. The difference in the calculated $\bar{C}_D$ is 23% in this 3-D case.

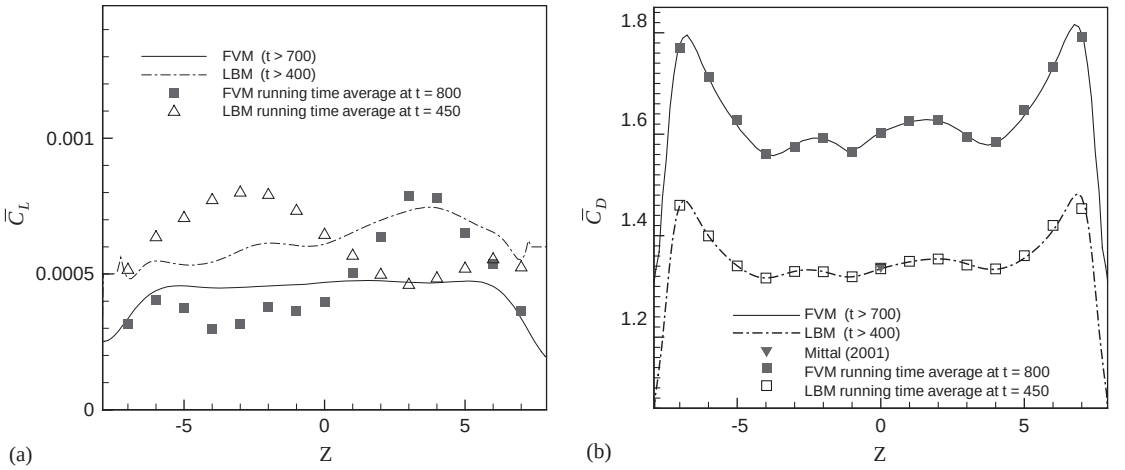

Fig. 15. Variation of $\bar{C}_L$ and $\bar{C}_D$ along cylinder span with Re = 100 and $a = 16$: (a) $\bar{C}_L$; (b) $\bar{C}_D$.

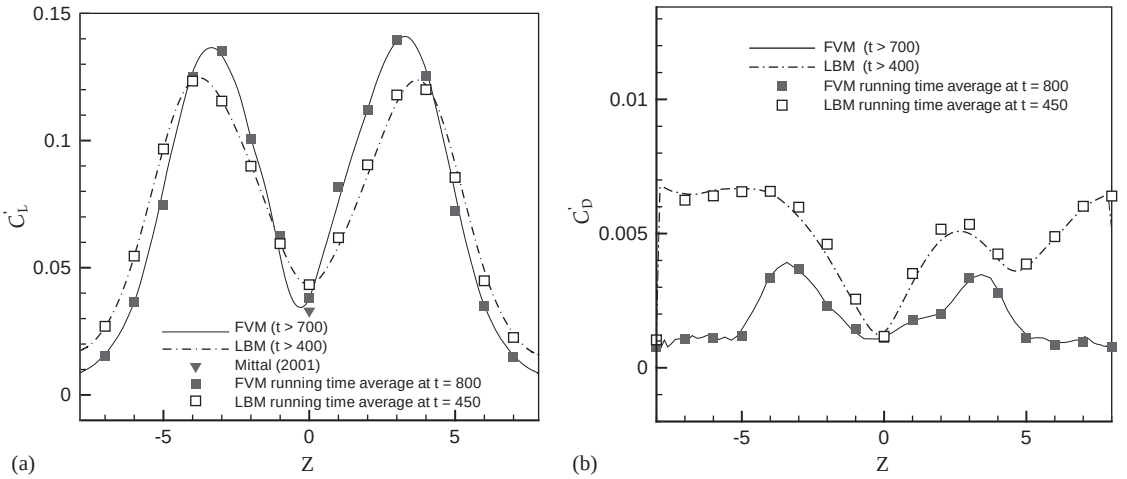

Fig. 16. Variation of C'_L and C'_D along cylinder span with Re = 100 and $a = 16$: (a) C'_L; (b) C'_D.

In general, $\bar{C}_D$ reaches a peak near the walls, and then displays a relatively flat distribution along the central $L/2$ span. Due to 3-D wake effect, the distribution is not exactly symmetric about midspan. The $\bar{C}_D$ data at midspan reported by Mittal (2001) is also plotted in Fig. 15(b) for comparison; it is in good agreement with the LBM result. The average $\bar{C}_D$ at midspan and over the entire span L is given in Table 1. With the exception of the FVM result, the present LBM calculated $\bar{C}_D$ and other reported calculations of $\bar{C}_D$ (Persillon and Braza, 1998; Zhang and Dalton, 1998) agree with the value $\bar{C}_D = 1.32 \pm 0.066$ (Table 1). This includes the present 2-D calculations derived from the FVM and LBM results and shows that $\bar{C}_D$ in the midspan of a 3-D cylinder is essentially similar to its 2-D counterpart. In view of this, it could be said that the LBM-calculated $\bar{C}_D$ is more in line with other reported values. The variation of the calculated $\bar{C}_D$ in the central $L/2$ region is very small and suggests that $\bar{C}_D$ measurements, which are normally derived from locations in the central $L/2$ region, are not sensitive to Z. These results partly explain why $\bar{C}_D$ measurements reported in the literature have been quite consistent for both 2-D and 3-D cylinders. The stationary nature of the C_D signal is substantiated by the good agreement shown between the time-average values and the RTA calculations across the entire span. This is true for both FVM and LBM calculations and lends credence to the claim that the discrepancies seen in the $\bar{C}_L$ plots are simply numerical calculation error.

The FVM and LBM calculated C'_L and C'_D along Z are plotted in Fig. 16 and the time average value over the entire span and midspan value of C'_L and C'_D are tabulated in Table 1 for comparison with other calculated and measured C'_L

and C'_D. A 2-D calculation has also been carried out to facilitate comparison with 3-D results. Essentially, the calculated $\bar{C}_L$ is zero (Fig. 15(a)); the error margin along the span is at least two orders of magnitude smaller than the calculated C'_L. This shows that either numerical method is suitable for this problem. The calculated C'_{L-2D} is within the range of the published C'_{L-2D} (Table 1). However, the calculated C'_{L-3D} reported in Zhang and Dalton (1998) is much higher than the present 3-D calculations; about 5–10 times larger. A possible reason could be the imposition of periodic boundary conditions at the ends of the cylinder. A periodic boundary condition presumes a certain period for the wake and induced-force behavior and that this behavior will repeat itself if the actual span of the cylinder is multiples of the assumed period. This is tantamount to prescribing a behavior for the wake and induced force. As will be shown in Section 4.8, where the effect of aspect ratio is investigated, an appropriate period could not be found in the range of a examined, $6 \leqslant a \leqslant 16$. It is in this sense that the periodic boundary condition can be considered as one that limits the development of the 3-D nature of the calculations. Consequently, the wall effect on the flow cannot be accounted for properly.

Most measurements have been carried out in wind or water tunnels where the cylinder spanned the entire cross-section on the test-section and the force was usually measured at midspan. In view of this, the present calculations could be compared with most reported measurements at the same Re. Therefore, the present C'_L results could be considered to be quite consistent with the measurements of Tanida et al. (1973). Note also the measurements of Khalak and Williamson (1996) at Re = 200–1300. Their measured C'_L vary from 0.03 to 0.30. The value at Re = 200 is in line with the present calculation and that of Mittal (2001). On the other hand, reported simulated C'_L results include C'_{L-2D} and C'_{L-3D} and, as summarized in Norberg (2003), fall within the range 0.11–0.52, with most investigations reporting a value around 0.24. The exception is the midspan value reported by Mittal (2001) for a 3-D calculation. This value, $C'_{L-3D} = 0.033$, is in line with the midspan values obtained by the present LBM and FVM calculations (Table 1). The calculated spanwise average value is about twice as large as the midspan value (Table 1); even then, it is not close to the lowest value summarized in Norberg (2003). Compared to the measurements of Tanida et al. (1973) and Khalak and Williamson (1996) at $\mathrm{Re} \leqslant 200$, the C'_{L-2D} and C'_{L-3D} values reported in the literature are substantially higher, about three to four times higher. This difference could be partially explained by examining Fig. 16(a). According to this plot, measurement at the midspan is the lowest. However, simulated results obtained by assuming periodic boundary condition might not be able to replicate this behavior.

The plots in Fig. 16(a) show significant variation of C'_L along Z and fair agreement between FVM and LBM results. This is true, irrespective of whether the average is determined from time averaging or from the RTA method. In fact, the agreement between the two sets of values is excellent, thus lending further support to the conclusion that the C_L time series is stationary. Comparing with the $\bar{C}_D$ shown in Fig. 15(b), the difference between the FVM and LBM calculations in terms of percentage is about the same. The C'_L distribution is almost symmetric about cylinder midspan. Near the walls, C'_L is at its minimum because the wall boundary layer tends to suppress vortex shedding. Two peaks in C'_L exist between the walls, thus indicating strong vortex shedding at these locations, which occur around $Z = \pm 4$ for the LBM result. There is a shift to a smaller Z for the FVM result though. A similar shift also exists for the minimum C'_L location. For LBM, the minimum occurs at midspan, but shifted to $Z = -0.4$ for FVM. The C'_L calculation of Mittal (2001) is also plotted in Fig. 16(a) for comparison. It agrees better with the FVM result. The experimental C'_L is very sensitive to the location where it is measured, especially in the central region. A slight error in the determination of the location could give rise to a rather significant error in the measured C'_L. For example, from the LBM calculation, C'_L at $Z = 0$ is 0.043. If the Z location is moved to 0.8, C'_L becomes 0.054, thus resulting in an error of 26%. The error shown by the FVM result is more than double this amount for about the same shift in Z. This could be the reason why there are so much scatter reported in the measured C'_L. This behavior contrasts with that of $\bar{C}_D$ which is not sensitive to Z as long as Z is located within the central $L/2$ span. There is also a substantial difference between the spanwise average C'_L and the local C'_L; the discrepancy could be as large as 100%.

The C'_D distribution along Z is shown in Fig. 16(b). The FVM calculated C'_D is symmetric about $Z = 0$, but the LBM result is not. Since both calculations give rise to oblique vortex shedding in the stationary state, this lack of symmetry for the LBM result could not be attributed to oblique vortex shedding. One possible reason could be the nonstationary nature of the LBM-calculated C_D signal. Again, there is a large variation of C'_D along the span and the minimum value occurs at midspan. The percentage difference between the minimum and the maximum value amounts to 300% for the FVM result and to more than 600% for the LBM result. This large variation along the span could explain why there is so much scatter in the reported measurements of C'_D. The RTA calculations from FVM results are in good agreement with the time-average values along the span. There are slight discrepancies for the LBM results; however, the discrepancies are very small. Judging from the discrepancies alone, it will be difficult to conclude that the LBM-calculated C_D signal is nonstationary. With the help of Fig. 14(b), it is reasonable to conclude that the LBM calculated C_D signal is at best approaching stationary state but has not reached stationarity yet.

4.7. Force correlation coefficient

It has been known that vortex shedding from nominally 2-D bluff body exhibits certain 3-D characteristics. An effective way of quantifying this three dimensionality is to calculate the spatial correlation along the span and the associated phase angle ϕ of the local fluctuating lift. In the present calculations, C_L is a function of Z and t, i.e., $C_L = C_L(Z, t)$. Therefore, spatial correlation and autocorrelation at a fixed spatial location can be examined. The cross-correlation coefficient γ_{ij} at delay time τ between spanwise locations i and j is

$$\gamma_{ij}(\tau) = \frac{\sum_t \{[C_L(Z_i, t+\tau)][C_L(Z_j, t)]\}}{\sqrt{\sum_t [C_L(Z_i, t+\tau)]^2}\sqrt{\sum_t [C_L(Z_j, t)]^2}}. \tag{30}$$

The coefficient γ_{ij} between $Z \approx 0$ and another Z along the span at zero time delay ($\tau = 0$) is shown in Fig. 17. Here, $Z \approx 0$ is selected at a location where the minimum C'_L occurs. The γ_{ij} result deduced from LBM bears a striking resemblance to that of the FVM. There is no correlated region, except for a very narrow region around $Z \approx 0$. The cross-correlation between $Z \approx 0$ and $Z < -2$ is very weak; however, the cross-correlation between $Z \approx 0$ and $Z > 4$ is negative and $\gamma_{ij} \approx -0.8$. In the central region, γ_{ij} decreases from 1 to about zero on the $-Z$ side and from 1 to -0.8 on the positive Z side. The widely varied γ_{ij} indicates that the 2-D assumption might not be correct at this a and Re. Furthermore, γ_{ij} is not symmetric about the midspan, indicating the inappropriateness of a symmetry assumption.

In order to quantify ϕ, the autocorrelation $\gamma_{ij}(\tau)$ is calculated with time delay τ in the range 0.01–15. The results for both FVM and LBM are plotted in Fig. 18. Three $\gamma_{ij}(\tau)$ with i specified at $Z = -4$ (this is the i location) and j selected at three different Z are presented; $\gamma_{12}(\tau)$ represents the autocorrelation with j selected at $Z = 0.7$, $\gamma_{13}(\tau)$ has j specified at $Z = 4$ and $\gamma_{14}(\tau)$ has j located $Z = 7.5$. These three locations are chosen to cover about half of the cylinder span. An inspection of this figure shows a strong periodic variation of $\gamma_{ij}(\tau)$ with τ. It can be seen that the period of all three autocorrelations is ~ 7.07 and the phase difference is 2π. The phase of these autocorrelations can be determined as follows. Taking $\gamma_{12}(\tau)$ as an example, it is clear that the autocorrelation reaches a maximum ($\gamma_{12}(\tau) \sim 1$) at $\tau = 2.80$; therefore, the phase of $\gamma_{12}(\tau)$ is about $2.80 \times 2\pi/7.07 = 0.79\pi$.

A plot of ϕ versus Z is shown in Fig. 19. In this plot, the reference location is again selected at $Z \approx 0$ where C'_L is a minimum. Both LBM and FVM calculations are shown. These results reveal an almost identical phase for the lift along the span. The phase angle of the lift force seems antisymmetric about the midspan. Furthermore, ϕ varies significantly in the region $-2 < Z < 5$, and gives rise to a maximum variation of $\phi \approx 1.3\pi$. Beyond this region, ϕ is nearly constant within $5 < Z < 8$, and the value is about 0.8π. The phase ϕ in the region $-8 < Z < -2$ is only -0.44π, and is essentially constant. Thus, vortex shedding is out of phase and antisymmetric in the two sides of the cylinder.

4.8. Aspect ratio effect

Most reported spatial correlations have been calculated from the measured fluctuating velocity behind the cylinder. For a cylinder with smaller a, the wake could be 2-D (Norberg, 2003) and the spanwise fluctuating forces and velocities could be highly correlated. In order to investigate the effect of a on the spatial correlation, γ_{ij} calculated from C_D and C_L are compared with those deduced from the wake velocities for different a. Several more calculations with the aspect ratios selected as $a = 6$, 8, 10, 12 and 14 have been carried out. The calculation for each case is made at $\mathrm{Re} = 100$ and is carried out to a dimensionless time way after the phase of the lift force has switched. Only the section of data after the lift has achieved stationary state is used to calculate the spatial correlations. A secondary objective of this set of calculations is to examine whether an appropriate period exists for a long slender cylinder in order to assess the validity or lack thereof of the assumption of a periodic boundary condition in the simulation of the flow and induced force on such a cylinder.

In view of the fact that a large amount of velocity data is generated for each a, a decision has to be made to focus on certain a values where the velocity data will be stored for later analysis. Judging from the behavior of the lift and drag spatial correlations, it appears that the case where $a = 10$, 12 and 14 should be examined in detail. Consequently, the velocity data for these three cases is stored for later analysis. Four locations are selected to monitor the velocity time series for all selected a; these points are located at A, B, C and D in the wake. Coordinates of the four points are defined in Table 2. The C_D and C_L time series are chosen from $Z = \pm 2$. The correlation coefficients γ_{ij} are then calculated from these time series, and their behavior is used to ascertain the 3-D nature or lack thereof of the wake and flow-induced forces. Other characteristics of the wake and flow-induced forces will not be examined in detail. In order to simplify the notation for γ_{ij} from this point on, $\gamma_{\mathrm{AB},L}$ $(0, 0, 4)$ and $\gamma_{\mathrm{AB},D}$ $(0, 0, 4)$ are used to denote γ_{ij} between $Z = \pm 2$ for the lift and drag force coefficient, respectively, and $\gamma_{ij,u}$ is used to denote γ_{ij} for the u velocity between AB and CD, or $\gamma_{\mathrm{AB},u}$ $(1.5, 0, 4)$ and $\gamma_{\mathrm{CD},u}$ $(1.5, 1.5, 4)$, respectively. Similar notations are used for the location CD and for the v velocity.

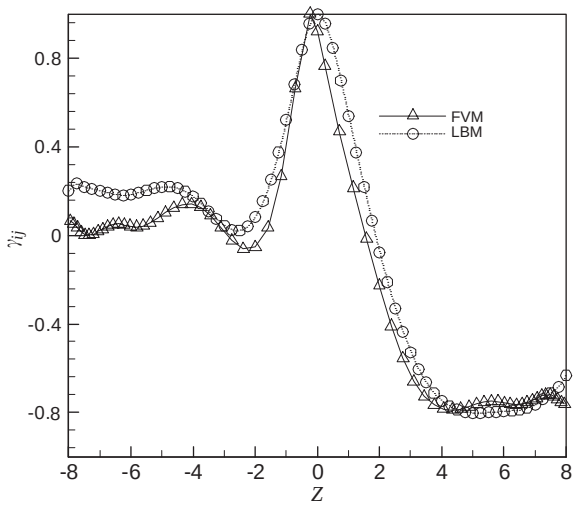

Fig. 17. Cross-correlation of C_L between the location of minimum C'_L and other locations of the span.

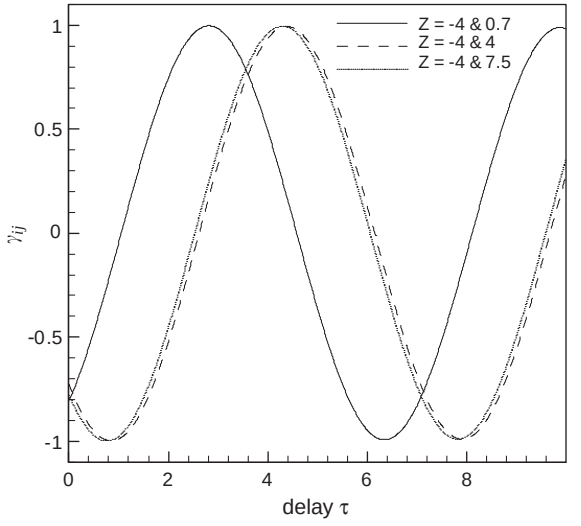

Fig. 18. Cross-correlation of C_L with τ delay between any two locations.

Variations of γ_{ij} with a are shown in Fig. 20. For $a = 10$, the values of $\gamma_{AB,L}$, $\gamma_{AB,D}$, $\gamma_{ij,u}$ and $\gamma_{ij,v}$ are essentially $+1$. The $\gamma_{ij,u}$ and $\gamma_{ij,v}$ determined from AB and CD are identical and equal to $\gamma_{AB,L}$ and $\gamma_{AB,D}$, thus indicating a 2-D wake behind the cylinder. At $a = 8$, $\gamma_{AB,D}$ is quite a bit lower than $\gamma_{AB,L}$. The reason could be attributed to the effect of either end (boundary layer) on C_D or to the less than stationary nature of the drag force. According to the studies of Berger and Wille (1972), Slaouti and Gerrard (1981), Gerich and Eckelmann (1982), and Stager and Eckelmann (1991), end plates have a significant effect on vortex shedding along the cylinder span. Therefore, it is not surprising that the flow-induced forces will be affected near the cylinder ends (see Figs. 15 and 16 for the peaks in $\tilde{C}_D$ and C'_L near the ends of the cylinder span). As a increases to 12, $\gamma_{AB,L}$ is still highly correlated ($\gamma_{AB,L} \approx +1$) and coincides with $\gamma_{ij,u}$ and $\gamma_{ij,v}$, but $\gamma_{AB,D}$ drops to nearly 0, thus indicating an increasing end effect on the flow-induced drag. At $a = 14$, $\gamma_{AB,L}$is nearly -1, indicating an antiphase vortex shedding between $Z = \pm 2$. This suggests that the wake has become 3-D at $a = 14$. Also, the behavior of $\gamma_{CD,u}$, $\gamma_{CD,v}$ and $\gamma_{AB,v}$ are consistent with $\gamma_{AB,L}$, indicating an antiphase correlation between $Z = \pm 2$.

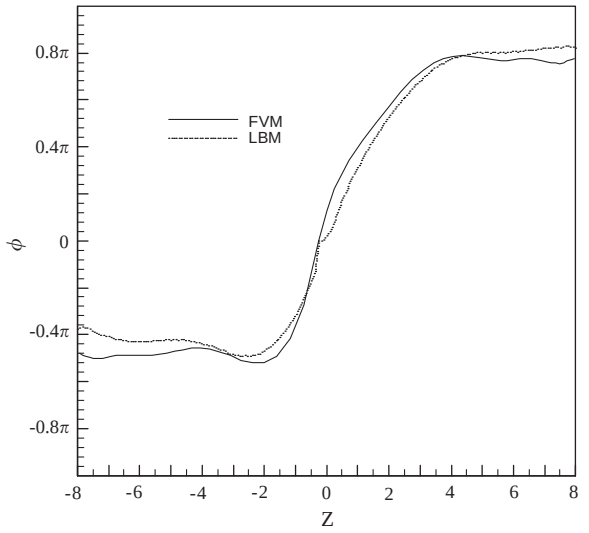

Fig. 19. Phase of C_L along cylinder span calculated using FVM and LBM.

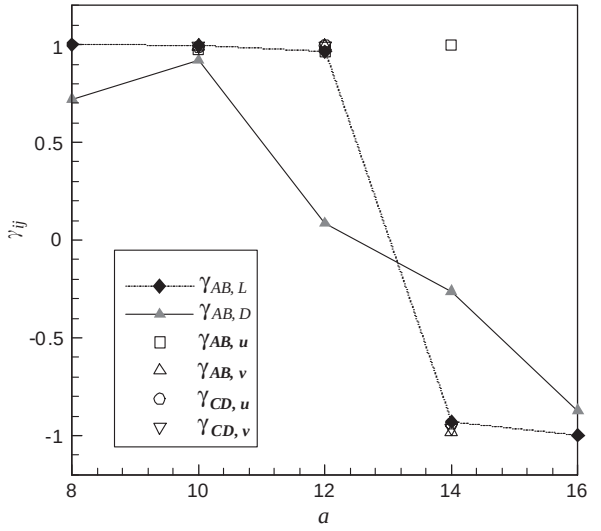

Fig. 20. Variation of γ_{ij} as a function of a at Re = 100.

However, $\gamma_{AB,u}$ is almost +1, suggesting an in-phase variation of the stream component velocity u between $Z = \pm 2$. Since points A and B are located at the $Y = 0$ plane, which is the symmetry plane of vortex shedding from cylinder top and bottom, it is most likely that A and B experience the same velocity variation with time. Consequently, the u velocity at these locations is highly correlated. On the other hand, $\gamma_{AB,D}$ is not as well correlated as $\gamma_{AB,L}$ even though its behavior is still determined by vortex shedding.

The results of $\gamma_{AB,L}$, $\gamma_{AB,D}$, $\gamma_{ij,u}$ and $\gamma_{ij,v}$ indicate that, at Re = 100, the nature of the wake flow is influenced by a. At $a = 10$, the wake is essentially 2-D, while for $a = 14$ the wake becomes 3-D. This behavior partially explains why 2-D wake was reported in the literature for Re = 100 because most a investigated was less than 16. For those simulations where $12 < a < 16$, the assumption of symmetry plane and/or periodic boundary condition was usually invoked. Consequently, the nature of the wake could not be properly investigated. In the present simulation, no such assumption

Table 2
Coordinates of the locations A, B, C, and D for the spatial correlation γ_{ij}

	A	B	C	D
X	1.5	1.5	1.5	1.5
Y	0	0	1.5	1.5
Z	2	−2	2	−2
γ_{ij}	γ_{AB} (1.5, 0, ±2)		γ_{CD} (1.5, 1.5, ±2)	

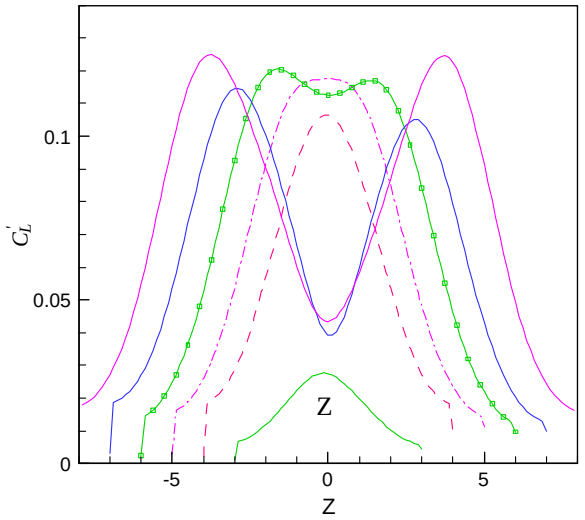

Fig. 21. Variation of C_L' along cylinder span for $6 \leqslant a \leqslant 16$ at Re = 100.

has been made concerning the wake flow. The wake is found to be 3-D for $a = 14$ and it is this character that causes the flow-induced forces to assume a 3-D behavior.

From Fig. 20, it can be seen that the flow-induced unsteady forces are also affected by a. In order to examine this effect further, the C_L' distributions along the span of the cylinder for the different cases are deduced and plotted in Fig. 21. There are six cases altogether. These six cases represent two different groups, with distinct behavior for each group. For $a \leqslant 10$, the C_L' distribution only shows one maximum and it is located at the midspan. As a increases to 12, two maxima start to appear, one on either side of the midspan and the C_L' value at midspan reaches a minimum. Further increasing a to 14 and 16 yields essentially the same behavior as that shown for $a = 12$, but the lowest C_L' value drops drastically. This lowest value does not seem to be affected much for $a \geqslant 14$. As a increases beyond 12, the locations of the maxima move toward the cylinder ends. The change from one type of behavior to the next is an indication of the extent of the end wall effect on vortex shedding and hence on the flow-induced forces. It appears that, for $a \geqslant 12$, the effect is confined to a region near the end walls and has not penetrated into the central core of the cylinder; hence, the existence of two peaks near the end walls. This C_L' distribution behavior does not support the assumption of periodic boundary conditions in a 3-D simulation of the flow and induced force on the cylinder. After all, within this range of a investigated, an appropriate period could not be identified for proper calculations to be carried out.

5. Conclusions

A long slender cylinder with two end plates in a cross-flow has been numerically simulated using FVM and LBM. The simulations were carried out for $6 \leqslant a \leqslant 16$ and at Re = 100. These choices are based on the knowledge that, according

to results reported in the literature, the wake at this Re is still 2-D and that the flow-induced forces are stationary. One of the objectives is to investigate whether these two points are true for all a examined. The computational results lead to the following conclusions:

(i) The FVM and LBM are used to simulate the 2-D case and the calculated $\bar{C}_D$ and C'_L are consistent with those reported in the literature. The difference between the FVM and LBM results is substantial and, in general, the FVM values are higher.

(ii) At $a = 16$, the wake is 3-D. Vortex shedding changes from a parallel behavior to an oblique behavior in the time range, $600 \leqslant t \leqslant 900$ (Fig. 4). Along the span, the lift contours become antiphase (Fig. 12). This phase shift occurs after a complete transition from quasi-stationary to stationary has taken place and $t > 730$. This oblique vortex shedding behavior in the stationary state is partially responsible for the 3-D flow-induced forces acting on the cylinder. As a result, the flow-induced forces vary substantially with Z and the cross-correlation of the lift force and its phase indicate a strong 3-D vortex shedding phenomenon and wake flow behind the cylinder.

(iii) For the 3-D case, the lift and drag signals are not stationary for a nondimensional time $t < 200$. The signals go through a transition period in the range $200 < t < 500$, where the signals appear to be stationary. This is true for FVM results only. For LBM results, the lift and drag signals do not show such a transition period, rather they continue to decrease with time until $t \approx 500$. Beyond $t \approx 500$, the signals decrease to another stationary state for FVM results and to a stationary state for LBM results. The stationary state for both LBM and FVM extends from $t = 500$ to 1500. The peak-to-peak values of the force signals decrease substantially from the first stationary state to the next for FVM. This variation partially explains why there are much scatter in the reported C'_L and C'_D, and casts doubt on previously reported values determined from numerical simulations terminated at $t \leqslant 500$.

(iv) The previously reported C'_L values (determined at $t = 200$–300) are close to that reported for the 2-D case. They are 5–10 times larger than the experimentally measured values (Tanida et al., 1973; Khalak and Williamson, 1996). Determining C'_L from the lift signal in the range $200 < t < 500$ could contribute to a high calculated C'_L and could partially explain the discrepancy between calculations and measurements.

(v) The lift and drag signals were found to be stationary for the FVM results; however, for the LBM results, even though the lift signal was stationary, the drag signal was not quite stationary because the C'_D was found to vary with time, albeit slightly, way after $\bar{C}_D$ was found to be independent of time. Two different methods were used to evaluate the time-mean values; a straightforward time-averaging method and the RTA method. In spite of this, the straightforward time-averaging values of $\bar{C}_D$ and C'_D are in good agreement with those deduced from RTA. In this sense, the drag signal could also be considered approaching stationarity.

(vi) The two numerical methods (FVM and LBM) studied can replicate the trend of the calculations correctly; however, their calculated results differ quantitatively. The LBM-calculated $\bar{C}_D$ and C'_L are in agreement with measurements, while the calculated $\bar{C}_D$ is also in agreement with other calculations. Other calculations give a value of C'_L that is substantially higher than the LBM result. This discrepancy could be partially explained by the assumption of a periodic boundary condition in their calculations. On the other hand, the FVM-calculated $\bar{C}_D$ is, in general, higher than the measured value, but the calculated C'_L is consistent with that given by the LBM and measurements.

(vii) Based on the range of a investigated, no clear pattern exists for the behavior of the spanwise C'_L distribution. The results do show that the spanwise C'_L distribution is very much affected by a. For $a \leqslant 12$, there is only one peak in the spanwise C'_L distribution and this change to one with two peaks as a increases beyond 12. It is evident from these results that no appropriate period can be found within the range of a examined. This implies that the periodic boundary conditions are not suitable for the simulation of 3-D flow around and induced-force acting on a cylinder in a cross-flow.

(viii) Present calculations do provide evidence to explain the wide scatter observed in the experimental measurements of C'_L, at least in the range of Re and a investigated.

Acknowledgments

Funding support given by the Research Grants Council of the Government of the HKSAR under Grant Nos. PolyU5166/01E, PolyU5172/02E, PolyU5307/03E and PolyU1/02C, and by the Hong Kong Polytechnic University under CRG No. A-PD75 is gratefully acknowledged.

References

Baban, F., So, R.M.C., 1991. Aspect ratio effect on flow-induced forces on circular cylinders in a cross flow. Experiments in Fluids 10, 313–321.

Berger, E., Wille, R., 1972. Periodic flow phenomena. Annual Review of Fluid Mechanics 4, 312–340.

Bhatnagar, P.L., Gross, E.P., Krook, M., 1954. A model for collision processes in gases, 1., small amplitude processes in charged and neutral one-component systems. Physical Review 94, 511–525.

Cercignani, C., 1988. The Boltzmann Equation and its Applications. Springer, New York.

Chan, K.T., Wang, X.Q., 1997. Free vibration of a Timoshenko beam partially loaded with distributed mass. Journal of Sound and Vibration 206, 353–369.

Chen, H.D., Chen, S.Y., Matthaeus, W.H., 1992. Recovery of the Navier–Stokes equations using a lattice-gas Boltzmann method. Physical Review A 45, 5339–5342.

Chilukuri, R., 1987. Incompressible laminar flow past a transversely vibrating cylinder. Journal of Fluids Engineering 109, 166–171.

Daubechies, I., 1990. The wavelet transform time–frequency localization and signal analysis. IEEE Transactions: Information Theory 36, 961–1004.

Eisenlohr, H., Eckelmann, H., 1989. Vortex splitting and its consequences in vortex street wake of cylinder at low Reynolds numbers. Physics of Fluids A 1, 189–192.

Evangelinos, C., Karniadakis, G.E., 1999. Dynamics and flow structures in the turbulent wake of rigid and flexible cylinders subject to vortex-induced vibrations. Journal of Fluid Mechanics 400, 91–124.

Farge, M., 1992. Wavelet transforms and their applications to turbulence. Annual Review of Fluid Mechanics 24, 395–457.

Gerich, D., Eckelmann, H., 1982. Influence of end plates and free ends on the shedding frequency of circular cylinder. Journal of Fluid Mechanics 122, 109–121.

Guo, Z., Shi, B.C., Wang, N.C., 2000. Lattice BGK model for incompressible Navier–Stokes equation. Journal of Computational Physics 165, 288–306.

Hama, F.R., 1957. Three-dimensional vortex patterns behind a circular cylinder. Journal of Aerospace Sciences 24, 156–157.

He, X., Doolen, G.D., 1997. Lattice Boltzmann method on a curvilinear coordinate system: vortex shedding behind a circular cylinder. Physical Review E 56, 434–440.

He, X.Y., Luo, L.-S., 1997a. A priori derivation of the lattice Boltzmann equation. Physical Review E 55 (Part A), R6333–R6336.

He, X.Y., Luo, L.-S., 1997b. Lattice Boltzmann model for the incompressible Navier–Stokes equation. Journal of Statistical Physics 88, 927–934.

Jordan, S.K., Fromm, J.E., 1972. Oscillatory drag, lift, and torque on a cylinder in a uniform flow. Physics of Fluids 15, 371–376.

Karniadakis, G.E., Triantafyllou, G.S., 1992. Three-dimensional dynamics and transition to turbulence in the wake of bluff objects. Journal of Fluid Mechanics 238, 1–30.

Khalak, A., Williamson, C.H.K., 1996. Dynamics of a hydroelastic cylinder with very low mass and damping. Journal of Fluids and Structures 10, 455–472.

Köng, M., Eisenlohr, H., Eckelmann, H., 1990. The fine structure in the S–Re relationship of the laminar wake of a circular cylinder. Physics of Fluids A 2, 1607–1611.

Matsumoto, M., 1999. Vortex shedding of bluff bodies: a review. Journal of Fluids and Structures 13, 791–811.

McNamara, G.R., Zanetti, G., 1988. Use of the Boltzmann equation to simulate lattice-gas automata. Physical Review Letters 61, 2332–2335.

Mei, R., Yu, D., Shyy, W., Luo, L.-S., 2002. Force evaluation in the lattice Boltzmann method involving curved geometry. Physical Review E 65, 041203-1-14.

Mittal, S., 2001. Computation of three-dimensional flows past circular cylinder of low aspect ratio. Physics of Fluids 13, 177–191.

Mittal, S., Balachandar, S., 1995. Effect of three dimensionality of the lift and drag of nominally two-dimensional cylinders. Physics of Fluids 7, 1841–1865.

Norberg, C., 1994. An experimental investigation of the flow around a circular cylinder: influence of aspect ratio. Journal of Fluid Mechanics 258, 287–316.

Norberg, C., 2003. Fluctuating lift on a circular cylinder: review and new measurements. Journal of Fluids and Structures 17, 57–96.

Persillon, H., Braza, M., 1998. Physical analysis of the transition to turbulence in the wake of a circular cylinder by three-dimensional Navier–Stokes simulation. Journal of Fluid Mechanics 365, 23–89.

Qian, Y.H., d'Humieres, D., Lallem, P., 1992. Lattice BGK models for Navier–Stokes equation. Europhysics Letters 17, 479–484.

Rhie, C.M., Chow, W.L., 1983. Numerical study of the turbulent-flow past an airfoil with trailing edge separation. AIAA Journal 21, 1525–1532.

Richter, A., Naudascher, E., 1976. Fluctuating forces on a rigid circular cylinder in confined flow. Journal of Fluid Mechanics 79, 561–576.

Roshko, A., 1954. On the drag and shedding frequency of two-dimensional bluff bodies NACA TN 3169.

Roshko, A., 1993. Perspectives on bluff body aerodynamics. Journal of Wind Engineering and Industrial Aerodynamics 49, 79–100.

Schafer, M., Turek, S., 1996. Benchmark computations of laminar flow around cyinder In: Hirschel, E.H. (Ed.), Flow Simulation with High-Performance Computers II, Notes on Numerical Fluid Mechanics, vol. 52, Vieweg, pp. 547–566.

Schlichting, H., 1955. In: Boundary Layer Theory. McGraw-Hill, New York, p. 16.

Slaouti, A., Gerrard, J.H., 1981. An experimental investigation of the end effects on the wake of a circular cylinder towed through water at low Reynolds numbers. Journal of Fluid Mechanics 112, 297–314.

So, R.M.C., Savkar, S.D., 1981. Buffeting forces on rigid circular cylinders in cross flows. Journal of Fluid Mechanics 105, 397–425.

So, R.M.C., Liu, Y., Chan, S.T., Lam, K., 2001. Numerical studies of a freely vibrating cylinder in a cross flow. Journal of Fluids and Structures 15, 845–866.

Stager, R., Eckelmann, H., 1991. The effects of endplates on the shedding frequency of circular cylinders in the irregular range. Physics of Fluids A 3, 2116–2121.

Szepessy, S., 1994. On the spanwise correlation of vortex shedding from a circular cylinder at high Reynolds number. Physics of Fluids 6, 2406–2416.

Szepessy, S., Bearman, P.W., 1992. Aspect ratio and end plate effects on vortex shedding from a circular cylinder. Journal of Fluid Mechanics 234, 191–217.

Tanida, Y., Okajima, A., Watanabe, Y., 1973. Stability of a circular cylinder oscillating in uniform flow or in a wake. Journal of Fluid Mechanics 61, 769–784.

Thompson, M., Hourigan, K., Sheridan, J., 1994. Three-dimensional instabilities in the cylinder wake. International Colloquium on Jet, Wakes, and Shear Layers, Melbourne, Australia.

Torrence, C., Combo, G.P., 1998. A practical guide to wavelet analysis. Bulletin of the American Meteorological Society 79, 61–78.

Tritton, D.J., 1959. Experiments on the flow past a circular cylinder at low Reynolds numbers. Journal of Fluid Mechanics 6, 547–567.

Wang, X.Q., So, R.M.C., Liu, Y., 2001. Flow-induced vibration of an Euler–Bernoulli beam. Journal of Sound and Vibration 243, 241–268.

West, G.S., Apelt, C.J., 1982. The effects of tunnel blockage and aspect ratio on the mean flow past a circular cylinder with Reynolds numbers between 10^4 and 10^5. Journal of Fluid Mechanics 112, 361–377.

Williamson, C.H.K., 1988. The existence of two stages in the transition to three-dimensionality of a cylinder wake. Physics of Fluids 31, 3165–3168.

Williamson, C.H.K., 1989. Oblique and parallel mode of vortex shedding in the wake of a cylinder at low Reynolds numbers. Journal of Fluid Mechanics 206, 579–627.

Williamson, C.H.K., 1992. The natural and forced formation of spot-like vortex dislocations in the transition of a wake. Journal of Fluid Mechanics 243, 393–441.

Williamson, C.H.K., 1996a. Vortex dynamics in the cylinder wake. Annual Review of Fluid Mechanics 28, 477–539.

Williamson, C.H.K., 1996b. Three-dimensional wake transition. Journal of Fluid Mechanics 328, 345–407.

Williamson, C.H.K., Roshko, A., 1988. Vortex formation in the wake of an oscillating cylinder. Journal of Fluids and Structures 2, 355–381.

Yu, D.Z., Mei, R.W., Shyy, W., 2002. A multi-block lattice Boltzmann method for viscous fluid flows. International Journal for Numerical Methods in Fluids 39, 99–120.

Zdravkovich, M.M., 1997 Flow around Circular Cylinders, vol. 1: Fundamentals. Oxford University Press, Oxford.

Zhang, J., Dalton, C., 1998. A three-dimensional simulation of a steady approach flow past a circular cylinder at low Reynolds number. International Journal of Numerical Methods in Fluids 26, 1003–1022.

Zhou, C.Y., So, R.M.C., Lam, K., 1999. Vortex-induced vibrations of an elastic circular cylinder. Journal of Fluids and Structures 13, 165–189.